ORIGINAL RESEARCH ARTICLE

Experimental Investigation and Thermodynamic Description of the Co–Nb–Zr System

JIAXING SUN, CUIPING GUO, CHANGRONG LI, and ZHENMIN DU

The liquidus surface projection and isothermal sections at 1100 and 1000 °C of the Co–Nb–Zr system were constructed by analyzing the solidification morphology of as-cast alloys and annealed microstructure of the equilibrated alloys and diffusion couples. Six primary solidification areas were obtained in the liquidus surface projection, and four primary solidification areas were deduced from the binary phase diagram. Additionally, three three-phase regions at 1100 °C and five three-phase regions at 1000 °C were determined in the isothermal sections. Based on the experimental information, a thermodynamic description of the Co–Nb–Zr system was established using the CALPHAD (CALculation of PHAse Diagram) method. The thermodynamic models of intermetallic phases $Co_{11}Zr_2$, $Co_{23}Zr_6$, $CoZr_2$, Co_7Nb_2, λ_1, λ_2 and λ_3, were described as $(Co)_{11}(Nb,Zr)_2$, $(Co)_{23}(Nb,Zr)_6$, $(Co,Zr)(Nb,Zr)_2$, Co_7Nb_2, $(Co,Nb)_2(Co,Nb)$, $(Co,Nb,Zr)_2(Co,Nb,Zr)$ and $(Co,Nb)_2(Co,Nb)$, respectively. $CoZr_3$ and μ were modeled as $(Co,Zr)(Co,Zr)Zr_2$ and $(Co,Nb,Zr)_1(Nb,Zr)_4(Co,Nb,Zr)_2(Co,Nb,Zr)_6$. Moreso, CoZr with the structure of B2 was described as an ordered phase of bcc_A2. Thus, a reasonable thermodynamic description of the Co–Nb–Zr system was obtained, and the experimental information was well reproduced.

https://doi.org/10.1007/s11661-023-07089-7

I. INTRODUCTION

Co-BASED alloys can be widely used in critical industrial materials such as magnetic materials and superalloys due to the addition of Nb, Ta, Mo, Ti, Zr, V, and other elements.[1–5] Additionally, Nb improves the stability of γ' and increases the volume fraction of $\gamma'(L1_2)$-precipitates.[6] Moreover, Nb can precipitate granular MC-type carbide at grain boundaries, improving the alloy's lasting strength.[7] However, acicular or flaky secondary carbides are precipitated at the grain boundaries by adding Nb, which decreases the alloy's plasticity and durability.[8] Additionally, Zr segregates at grain boundaries to reduce defects, thereby improving the strength and ductility of as-cast alloys.[9] Zr can also form MC-type carbides in Co-based superalloys, effectively strengthening the alloy matrix.[10] Notably, the atomic radii of Zr and Nb are close, and Nb and Zr with the same bcc structure can form an infinite solid solution bcc(Nb, Zr). Thus, alloys containing Nb and Zr have excellent corrosion resistance.[11] Therefore, it is essential for the phase relationships of the Co–Nb–Zr system to understand the phase stability and transformation in Co-based alloys with the addition of Nb and Zr.

The current work mainly investigates the phase relationships at 1100 and 1000 °C and the liquidus surface projection. The CALPHAD (CALculation of PHAse Diagram) method[12] is one of the efficient ways of material design. A thermodynamic description of the Co–Nb–Zr system by CALPHAD was performed, and the experimental information was reproduced with the obtained thermodynamic parameters. Importantly, the reasonable thermodynamic description of the Co–Nb–Zr system is integral to constructing a multicomponent thermodynamic database of Co-based superalloys.

II. LITERATURE INFORMATION

A. *The Co–Nb System*

In the Co–Nb system, there are five intermetallics Co_7Nb_2, Co_3Nb (λ_3), Co_2Nb (λ_2), $Co_{16}Nb_9$ (λ_1), and Co_7Nb_6 (μ).[13] Stein *et al.*[14] studied the Co–Nb system from 800 to 1380 °C utilizing diffusion couples and equilibrium alloys, and found that the compositions of Nb in the Laves phases of λ_3, λ_2, and λ_1 ranged from 24.5 to 25.5 at. pct, 26 to 35.3 at. pct, and 35.8 to 37.4 at. pct, respectively. Subsequently, several scholars

JIAXING SUN, CUIPING GUO, CHANGRONG LI, and ZHENMIN DU are with the Department of Materials Science and Engineering, University of Science and Technology Beijing, Beijing 100083, P.R. China. Contact e-mail: duzm@ustb.edu.cn, cpguo@ustb.edu.cn
Manuscript submitted February 7, 2023; accepted May 3, 2023.
Article published online May 28, 2023

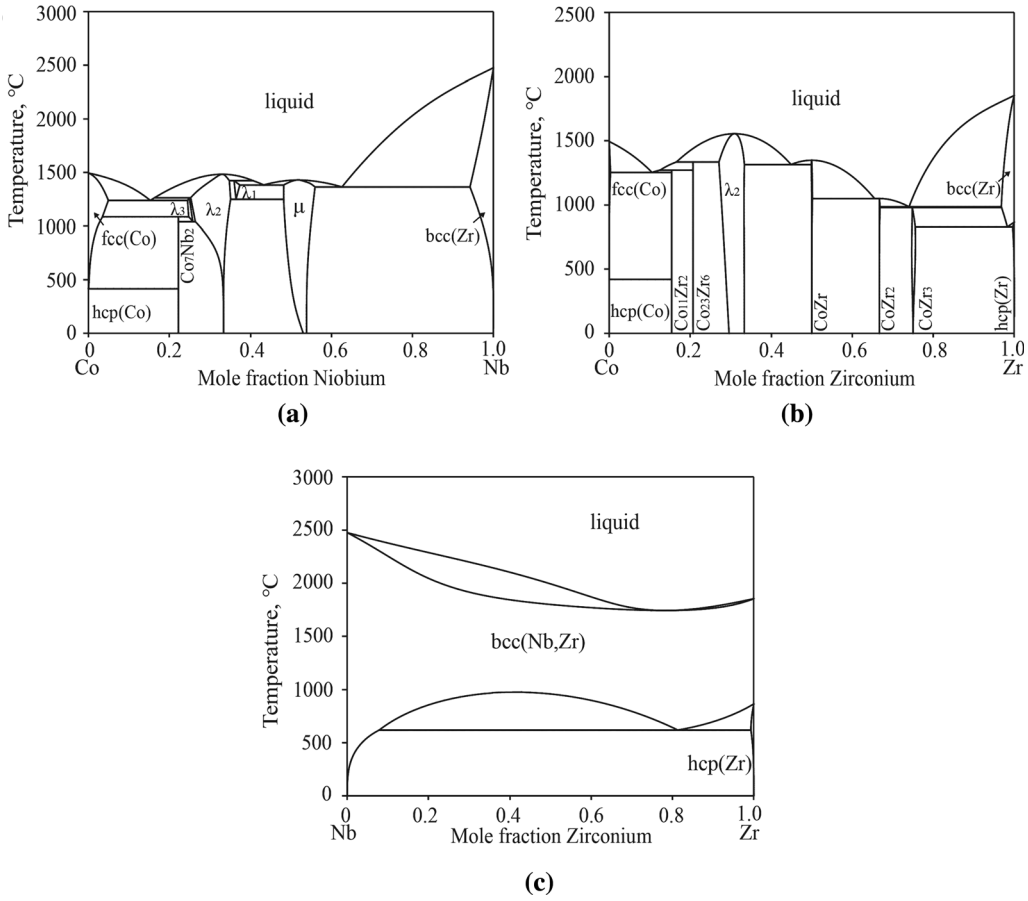

Fig. 1—Binary phase diagrams: (*a*) Co–Nb system[19]; (*b*) Co–Zr system modified in this work; (*c*) Nb–Zr system.[29] Reprinted from Refs. [19] and [29] with permission from Elsevier.

Table I. Crystallographic Data of Individual Compounds in the Co–Nb–Zr System

System	Phase	Strukturbericht	Person symbol	Space group	Prototype	References
Co–Nb	Co_7Nb_2	—	*mS*36	*mC*18	Ni_7Zr_2	[14]
	λ_1	C14	*hP*12	$P6_3/mmc$	$MgZn_2$	[13]
	λ_2	C15	*cF*24	$Fd\bar{3}m$	Cu_2Mg	[13]
	λ_3	C36	*hP*24	$P6_3/mmc$	$MgNi_2$	[13]
	μ	$D8_a$	*hR*39	$R\bar{3}m$	Fe_7W_6	[13]
Co–Zr	$Co_{11}Zr_2$	—	—	*Pcna*	—	[20]
	$Co_{23}Zr_6$	$D8_a$	*cF*116	$Fm\bar{3}m$	$Mn_{23}Th_6$	[20]
	Co_2Zr	C15	*cF*24	$Fd\bar{3}m$	Cu_2Mg	[20]
	CoZr	B2	*cP*2	$Pm\bar{3}m$	CsCl	[20]
	$CoZr_2$	C15	*cF*96	$Fm\bar{3}m$	Ti_2Ni	[20]
	$CoZr_3$	$D0_{19}$	*hP*2	$P6_3/mmc$	Mg_3Cd	[20]

conducted the thermodynamic optimization of the Co–Nb binary phase diagram.[15–19] Furthermore, the thermodynamic optimization of the Co–Nb system was re-evaluated while evaluating the ternary system Co–Nb–Ti by Wei *et al.*,[19] which was able to match the Co-based superalloy thermodynamic database, and adopted in this work. The calculated Co–Nb phase diagram is exhibited in Figure 1(a).

B. *The Co–Zr System*

The Co–Zr phase diagram was first studied by Pechin *et al.*,[20] and they identified five compounds $Co_{11}Zr_2$, $Co_{23}Zr_6$, Co_2Zr (λ_2), CoZr, and $CoZr_2$. Bataleva *et al.*[21] investigated the Co–Zr system and found the existence of $CoZr_3$ by using metallography, EPMA, and XRD methods. More recently, Liu *et al.*[22] found that the temperature of peritectoid reaction bcc(Zr) + $CoZr_2$ ↔ $CoZr_3$ was about 985 °C by using DTA (Differential

Table II. Primary Solidification Phases and Their Solidification Paths of the Co–Nb–Zr As-Cast Alloys

No.	Measured Alloy Compositions (at. Pct)			Primary Solidification Phases	Phase Compositions (at. Pct)			Solidification Paths
	Co	Nb	Zr		Co	Nb	Zr	
a1	91.2	2.1	6.7	fcc(Co)	98.8	1.1	0.1	liq. → fcc(Co) liq. → fcc(Co) + $Co_{23}Zr_6$
a2	90.4	4.3	5.3	fcc(Co)	97.4	2.3	0.3	liq. → fcc(Co) liq. → fcc(Co) + $Co_{23}Zr_6$
a3	92.7	5.6	1.7	fcc(Co)	96.4	3.5	0.1	liq. → fcc(Co) liq. → fcc(Co) + λ_2
a4	79.8	3.3	16.9	λ_2	76.5	3.2	20.3	liq. → λ_2 liq. + λ_2 → $Co_{23}Zr_6$
a5	82.8	5.9	11.3	λ_2	76.5	7.7	15.8	liq. → λ_2 liq. + λ_2 → $Co_{23}Zr_6$ liq. → $Co_{23}Zr_6$ liq. → fcc(Co) + $Co_{23}Zr_6$
a6	81.9	8.5	9.6	λ_2	75.8	13.0	11.2	liq. → λ_2 liq. → fcc(Co) + λ_2
a7	82.1	5.9	12.0	λ_2	76.7	15.2	8.1	liq. → λ_2 liq. + λ_2 → $Co_{23}Zr_6$ liq. → $Co_{23}Zr_6$ liq. → fcc(Co) + $Co_{23}Zr_6$
a8	81.7	3.1	15.2	λ_2	78.4	17.5	4.1	liq. → λ_2 liq. → fcc(Co) + λ_2 liq. → $Co_{23}Zr_6$ liq. → fcc(Co) + $Co_{23}Zr_6$
a9	80.3	18.6	1.1	λ_2	82.7	18.6	1.7	liq. → λ_2 liq. → fcc(Co) + λ_2
a10	75.3	3.9	20.8	λ_2	75.8	4.2	20.0	liq. → λ_2 liq. + λ_2 → $Co_{23}Zr_6$
a11	75.2	6.0	18.8	λ_2	71.7	7.0	21.3	liq. → λ_2 liq. + λ_2 → $Co_{23}Zr_6$
a12	75.4	16.2	8.4	λ_2	72.0	18.6	9.4	liq. → λ_2 liq. → fcc(Co) + λ_2
a13	75.2	10.6	14.2	λ_2	75.5	10.2	14.3	liq. → λ_2 liq. → fcc(Co) + λ_2
a14	74.9	9.1	16.0	λ_2	73.6	10.0	16.4	liq. → λ_2 liq. + λ_2 → $Co_{23}Zr_6$
a15	75.4	5.4	19.2	λ_2	78.0	5.2	16.8	liq. → λ_2 liq. → fcc(Co) + λ_2
a16	75.0	3.4	21.6	λ_2	76.5	3.4	20.1	liq. → λ_2 liq. + λ_2 → $Co_{23}Zr_6$
a17	56.6	3.6	39.8	λ_2	63.9	2.6	33.5	liq. → λ_2 liq. → CoZr + λ_2
a18	58.2	6.5	35.3	λ_2	63.2	5.0	31.8	liq. → λ_2 liq. → CoZr + λ_2
a19	65.0	21.1	13.9	λ_2	63.3	19.5	17.2	liq. → λ_2 liq. → μ + λ_2
a20	63.8	16.9	19.3	λ_2	63.3	15.4	21.3	liq. → λ_2 liq. → μ + λ_2
a21	66.5	25.2	8.3	λ_2	57.0	27.5	15.5	liq. → λ_2 liq. → μ + λ_2
a22	40.2	3.6	56.2	CoZr	48.2	2.0	49.8	liq. → CoZr liq. → CoZr + $CoZr_2$
a23	40.0	5.9	54.1	CoZr	47.8	2.6	49.6	liq. → CoZr liq. → CoZr + $CoZr_2$
a24	39.5	10.6	49.9	CoZr	47.4	4.7	47.9	liq. → CoZr liq. → CoZr + $CoZr_2$
a25	39.5	15.5	45.0	CoZr	48.1	6.8	45.1	liq. → CoZr liq. → bcc(Nb,Zr) + CoZr liq. → bcc(Nb,Zr) + CoZr + $CoZr_2$

Table II. continued

No.	Measured Alloy Compositions (at. Pct)			Primary Solidification Phases	Phase Compositions (at. Pct)			Solidification Paths
	Co	Nb	Zr		Co	Nb	Zr	
a26	40.0	20.0	40.0	CoZr	45.4	12.0	41.6	liq. → CoZr liq. → bcc(Nb,Zr) + CoZr liq. → bcc(Nb,Zr) + CoZr + $CoZr_2$
a27	53.3	15.5	31.2	λ_2	65.3	8.4	26.4	liq. → μ liq. → CoZr + μ liq. → CoZr + λ_2 + μ
a28	51.9	17.8	30.3	λ_2	63.7	10.6	25.7	liq. → μ liq. → CoZr + μ liq. → CoZr + λ_2 + μ
a29	57.1	24.2	18.7	μ	36.5	33.2	30.3	liq. → μ liq. → λ_2 + μ
a30	56.4	33.4	10.2	μ	55.4	30.9	13.7	liq. → μ liq. → λ_2 + μ
a31	55.9	38.7	5.4	μ	59.2	36.5	4.3	liq. → μ liq. → λ_2 + μ
a32	56.7	41.1	2.2	μ	50.4	48.3	1.3	liq. → μ liq. → λ_2 + μ
a33	45.9	39.8	14.3	μ	41.3	44.2	14.5	liq. → μ liq. → bcc(Nb,Zr) + μ
a34	47.1	43.7	9.2	μ	41.6	30.9	27.5	liq. → μ liq. → bcc(Nb,Zr) + μ
a35	48.5	46.1	5.4	μ	41.0	34.5	24.5	liq. → μ
a36	38.5	46.3	15.2	μ	41.8	47.4	10.8	liq. → μ liq. → bcc(Nb,Zr) + μ
a37	39.2	49.7	11.1	μ	42.3	50.6	7.1	liq. → μ liq. → bcc(Nb,Zr) + μ
a38	39.2	53.3	7.5	μ	41.7	52.7	5.6	liq. → μ liq. → bcc(Nb,Zr) + μ
a39	39.9	55.7	4.4	μ	41.9	54.3	3.8	liq. → μ liq. → bcc(Nb,Zr) + μ
a40	26.2	5.0	68.8	$CoZr_2$	28.2	8.0	63.8	liq. → $CoZr_2$ liq. → bcc(Nb,Zr) + $CoZr_2$
a41	26.9	9.5	63.6	$CoZr_2$	27.9	10.5	65.6	liq. → $CoZr_2$ liq. → bcc(Nb,Zr) + $CoZr_2$
a42	21.0	16.6	62.3	bcc(Nb,Zr)	5.5	42.6	51.9	liq. → bcc(Nb,Zr) liq. → bcc(Nb,Zr) + $CoZr_2$
a43	20.8	27.3	51.8	bcc(Nb,Zr)	3.7	69.8	26.5	liq. → bcc(Nb,Zr) liq. → bcc(Nb,Zr) + $CoZr_2$
a44	19.7	36.3	44.0	bcc(Nb,Zr)	3.0	83.2	13.8	liq. → bcc(Nb,Zr) liq. → bcc(Nb,Zr) + $CoZr_2$
a45	18.5	50.2	31.3	bcc(Nb,Zr)	2.4	86.8	10.8	liq. → bcc(Nb,Zr) liq. → bcc(Nb,Zr) + CoZr liq. → bcc(Nb,Zr) + CoZr + $CoZr_2$
a46	15.9	65.2	18.9	bcc(Nb,Zr)	2.9	90.8	6.3	liq. → bcc(Nb,Zr) liq. → bcc(Nb,Zr) + μ
a47	18.9	72.6	8.5	bcc(Nb,Zr)	4.8	91.1	4.1	liq. → bcc(Nb,Zr) liq. → bcc(Nb,Zr) + μ
a48	20.6	75.0	4.4	bcc(Nb,Zr)	5.8	93.5	0.7	liq. → bcc(Nb,Zr) liq. → bcc(Nb,Zr) + μ

Thermal Analysis). Subsequently, many researchers assessed the thermodynamic parameters of the Co–Zr system.[23–27] Moreso, Durga and Kumar[23] first adopted an order–disorder model to couple bcc_A2 and CoZr with B2 structure, thereby improving the thermodynamic parameters of the Co–Zr system. To make $G^{\lambda_2}_{Co:Co}$ in the Co–Zr system consistent with $G^{\lambda_2}_{Co:Co}$ in the Co-Nb system, the thermodynamic parameters of λ_2 in Reference 27 were re-optimized in this study. The calculated Co–Zr phase diagram is shown in Figure 1(b).

C. *The Nb–Zr System*

Guillermet[28] obtained the thermodynamic parameters of the Nb–Zr system based on analytical and experimental information. Recently, the thermodynamic parameters of the Nb–Si–Zr ternary system were

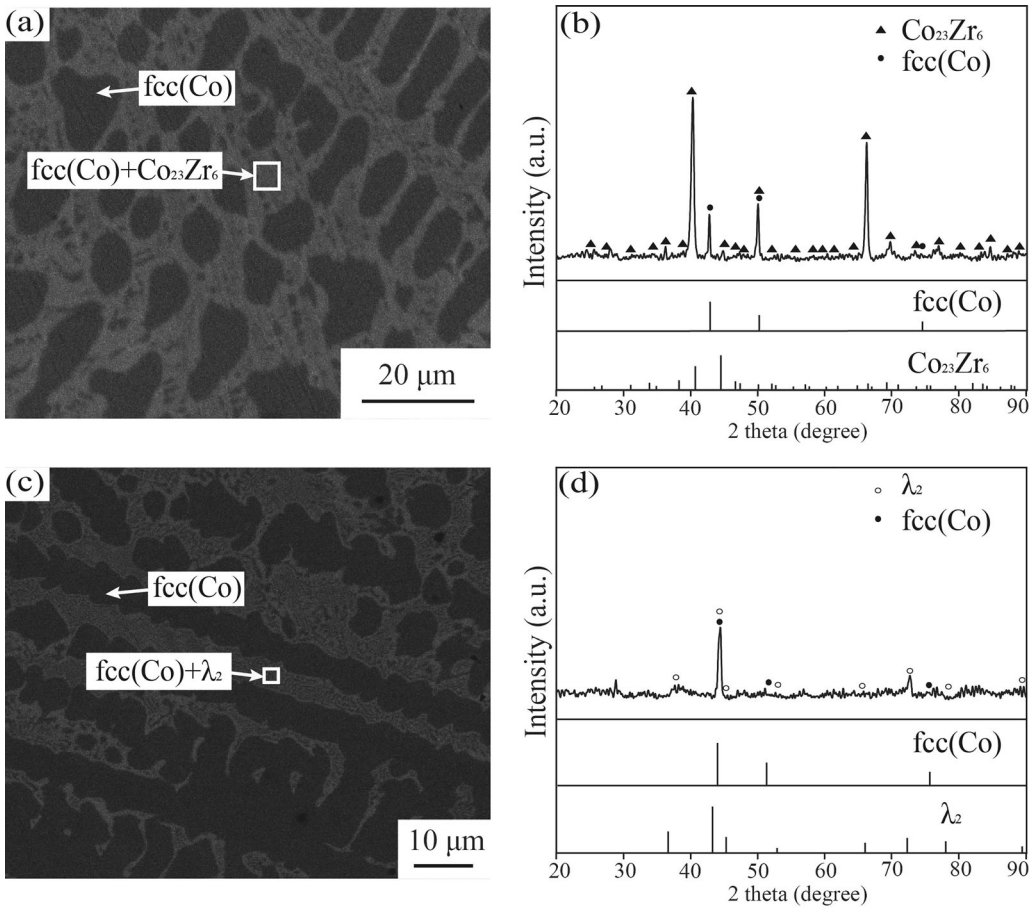

Fig. 2—BSE micrographs and XRD patterns of as-cast alloys: (*a*) and (*b*) a1; (*c*) and (*d*) a3.

evaluated by Li *et al*.[29] and were used in this work. The calculated Nb–Zr phase diagram is displayed in Figure 1(c). Furthermore, the crystallographic information of each compound in the Co–Nb–Zr system is outlined in Table I.

III. EXPERIMENTAL PROCEDURES

A. *Equilibrated Alloy Preparation*

High-purity cobalt, niobium, and zirconium (99.99 wt. pct) were used as the raw materials for the as-cast and annealed samples. Each specimen of about 3 g was melted by arc melting (MTI MSM20-7) under the protection of a high-purity argon atmosphere. Pure titanium was used as an oxygen absorber and should be remelted thrice before smelting, and then the samples were smelted at least six times. Under the atmosphere of high-purity argon as the protective gas, the as-cast alloys were encapsulated in quartz tubes. The annealing times of alloys b1–b9, alloys b10–b17 and alloys b18–b23 were 40, 80 and 2 days at 1100 °C, respectively. Additionally, the annealing times of the alloys c1–c8, alloys c9–c17 and alloys c18–c23 were 50, 90 and 3 days at 1000 °C, respectively. Furthermore, the specimens were quenched into ice water following heat treatment.

B. *Diffusion Couple Preparation*

Even if a long heat treatment time was used, achieving equilibrium is difficult when some refractory elements are contained. The diffusion couple method has been used as an efficient method to study phase equilibrium based on the principle of local equilibrium.[30] Therefore, to further verify the phase relationships of the Co–Nb–Zr system obtained with the equilibrium alloy at 1000 °C, the diffusion couple method was used. The as-cast Nb80Zr20 (at. pct) alloy obtained by smelting was cut into the blocks of 5 mm × 5 mm × 8 mm and annealed at 1200 °C for 108 hours. Subsequently, the contacting surfaces for Nb80Zr20 and Co were metallographically polished and tied together with Mo wire to form a block of diffusion couples. Moreso, the Nb80Zr20/Co diffusion couple was encapsulated in a quartz tube and then annealed at 1000 °C for 360 hours. Finally, the diffusion couple was quenched in ice water.

C. *Sample Analysis*

The heat-treated samples were subjected to metallographic analysis under a scanning electron microscope (SEM) equipped with an energy dispersive spectrometer (EDS) at an accelerating voltage of 20.0 kV to determine the microstructures and phase compositions. Additionally, an XRD instrument obtained the XRD

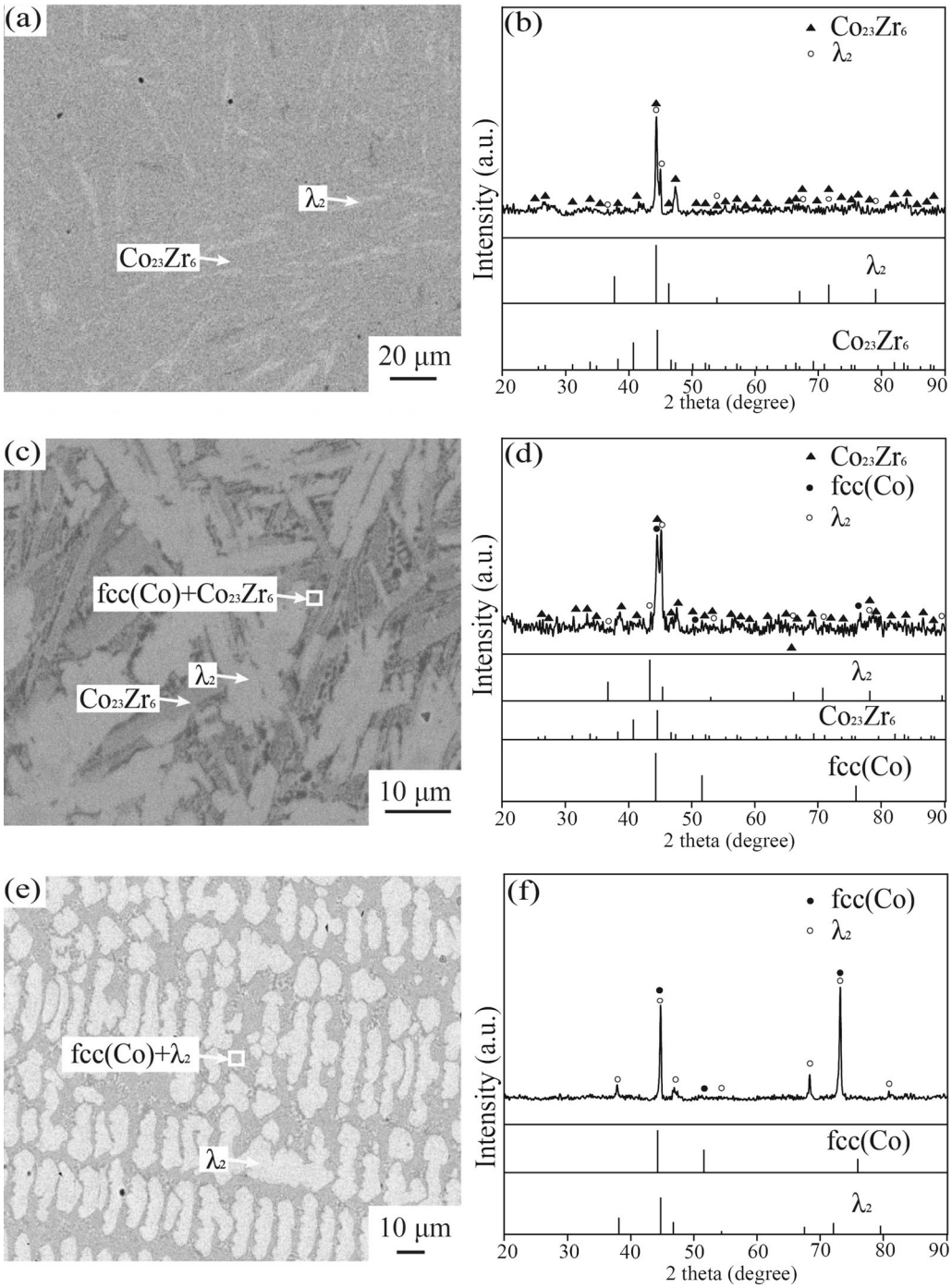

Fig. 3—BSE micrographs and XRD patterns of as-cast alloys: (*a*) and (*b*) a4; (*c*) and (*d*) a5; (*e*) and (*f*) a9.

patterns of the specimens. Notably, the diffraction pattern has a scan step size of 0.02 deg in the 2θ range from 20 to 90 deg. Furthermore, EPMA-1720H (Shimadzu, Japan) with a wave dispersive X-ray spectrometer (WDS) was used to measure the phase equilibria between fcc(Co), λ_2, μ, CoZr, and bcc(Nb, Zr) in the Nb80Zr20/Co diffusion couple.

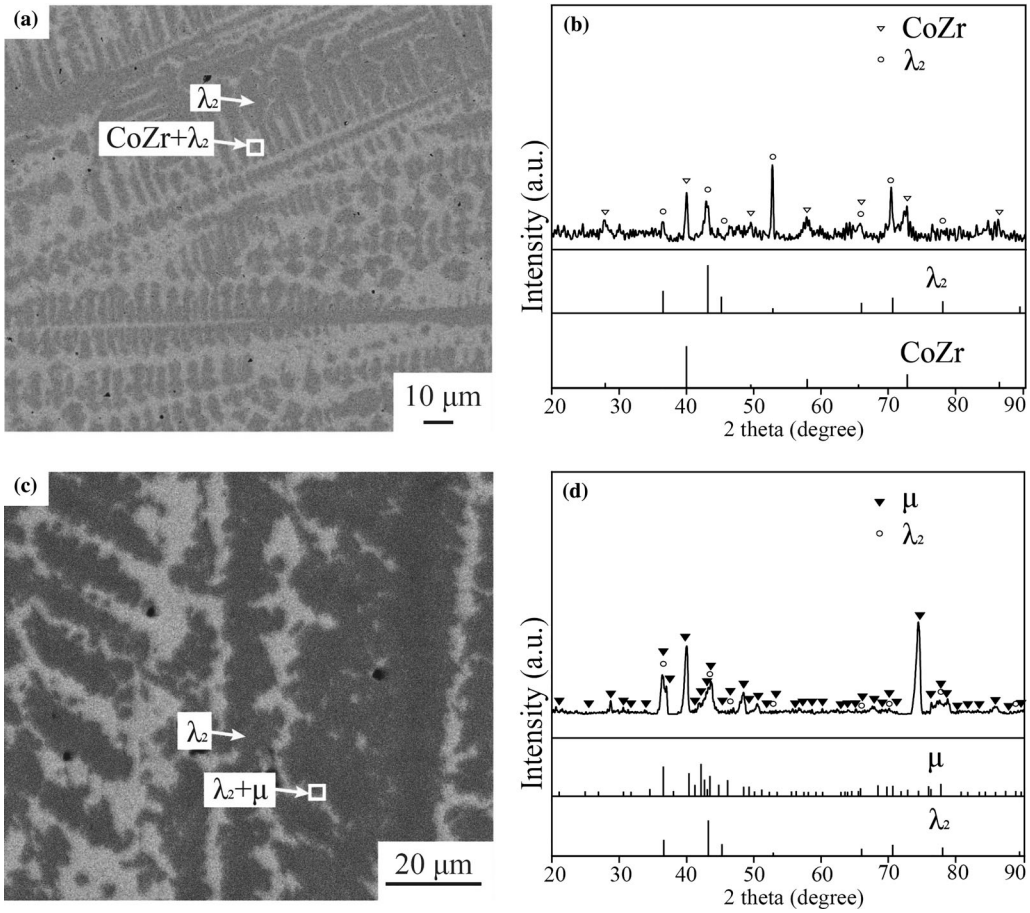

Fig. 4—BSE micrographs and XRD patterns of as-cast alloys: (*a*) and (*b*) a17; (*c*) and (*d*) a19.

IV. RESULTS AND DISCUSSION

A. *Liquidus Surface Projection*

The primary solidification phase and the solidification paths of 48 alloys are displayed in Table II. The solidification paths of typical as-cast alloys are selected for discussion.

The primary solidification phase is fcc(Co) in alloys a1 to a3. Combined with the XRD pattern of alloy a1 in Figure 2(b), only two phases fcc(Co) and $Co_{23}Zr_6$ were determined. The black phase fcc(Co) as the primary solidification phase was observed in Figure 2(a). Moreso, fcc(Co) was first precipitated from the liquid phase, and the composition of the remaining liquid phase was at the univariate line of liq. $\rightarrow$ fcc(Co) + $Co_{23}Zr_6$. The microstructure and XRD patterns of alloy a3 are displayed in Figures 2(c) and (d), where the black phase fcc(Co) as the primary solidification phase and a eutectic structure fcc(Co) + λ_2 were observed. Thus, there must be a monovariant line of liq. $\rightarrow$ fcc(Co) + λ_2 between fcc(Co) and λ_2 in the liquidus surface projection.λ_2 as the primary solidification region was observed in alloys a4 to a21. However, the solidification structure is completely different due to the different solidification paths after λ_2 precipitation. Alloys a4, a10, a11, a14, and a16 have the same solidification path. The microstructure and XRD patterns of alloy a4 are exhibited in Figures 3(a) and (b), where the phases λ_2 and $Co_{23}Zr_6$ were determined. λ_2 was first precipitated, and the liquid composition was at the univariate line of liq. + $\lambda_2 \rightarrow$ $Co_{23}Zr_6$. Notably, alloys a5, a7, and a8 have identical solidification paths. Three phases, λ_2, $Co_{23}Zr_6$, and fcc(Co), were determined according to the XRD pattern of alloy a5, as shown in Figure 3(d). The light phase λ_2, the grey phase $Co_{23}Zr_6$, and a eutectic microstructure fcc(Co) + $Co_{23}Zr_6$ are shown in Figure 3(c). λ_2 was first precipitated from the liquid phase, and the composition of the liquid was at the peritectic univariate line of liq. + $\lambda_2 \rightarrow Co_{23}Zr_6$. Then the remaining liquid phase moved to the monovariant line and transformed into fcc(Co) + $Co_{23}Zr_6$ microstructure. The solidification path can be surmised: liq. $\rightarrow \lambda_2$, liq. + $\lambda_2 \rightarrow Co_{23}Zr_6$, liq. $\rightarrow Co_{23}Zr_6$ and liq. $\rightarrow$ fcc(Co) + $Co_{23}Zr_6$. Moreso, alloys a6, a9, a12, a13, and a15 have identical solidification paths. The microstructure and XRD patterns of alloy a9 are exhibited in Figures 3(e) and (f). λ_2 was first precipitated from the liquid phase, and the composition of the liquid was at the univariate line of liq. $\rightarrow$ fcc(Co) + λ_2. As shown in Figure 4(b), CoZr and λ_2 were detected based on the XRD pattern of alloy a17. The dark phase λ_2 and the light phase CoZr were observed as shown in Figure 4(a). A eutectic microstructure CoZr + λ_2 was formed from the liquid phase after the precipitation of λ_2. The microstructure and XRD

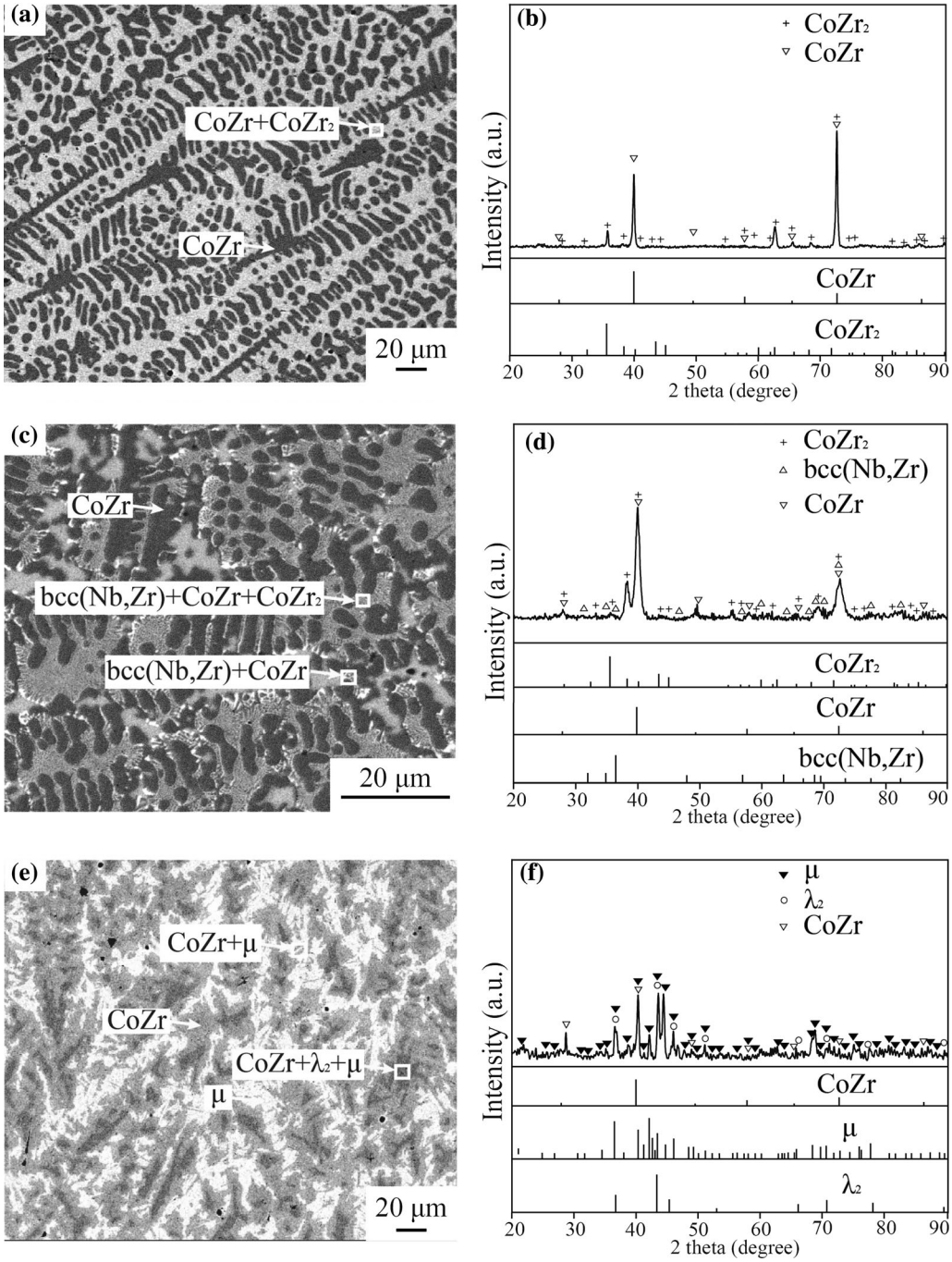

Fig. 5—BSE micrographs and XRD patterns of as-cast alloys: (*a*) and (*b*) a22; (*c*) and (*d*) a25; (*e*) and (*f*) a27.

patterns of alloy a19 are exhibited in Figures 4(c) and (d), where the black phase λ_2 and the light phase μ were observed. λ_2 was precipitated at the beginning, and then the remaining liquid phase moved to the monovariant line and transformed into $\lambda_2 + \mu$ microstructure.

Alloys a22 to a26 have the same primary solidification phase as CoZr. The microstructure and XRD patterns of alloy a22 are exhibited in Figures 5(a) and (b), where CoZr and $CoZr_2$ were observed. CoZr was first precipitated from the liquid phase, and the composition of the remaining liquid phase was at the univariate line of liq. $\rightarrow$ CoZr + $CoZr_2$. Only three phases, bcc(Nb, Zr), CoZr, and $CoZr_2$, were detected from the XRD patterns of alloy a25 in Figure 5(d). A eutectic microstructure bcc(Nb, Zr) + CoZr and a ternary eutectic microstructure bcc(Nb, Zr) + CoZr + $CoZr_2$ were observed in Figure 5(c). The solidification path can be conjectured: liq. $\rightarrow$ CoZr, liq. $\rightarrow$ bcc(Nb, Zr) + CoZr and liq. $\rightarrow$ bcc(Nb, Zr) + CoZr + $CoZr_2$.

The primary solidification region of μ was observed in alloys a27 to a39. The microstructure and XRD patterns of alloy a27 are displayed in Figures 5(e) and (f), where

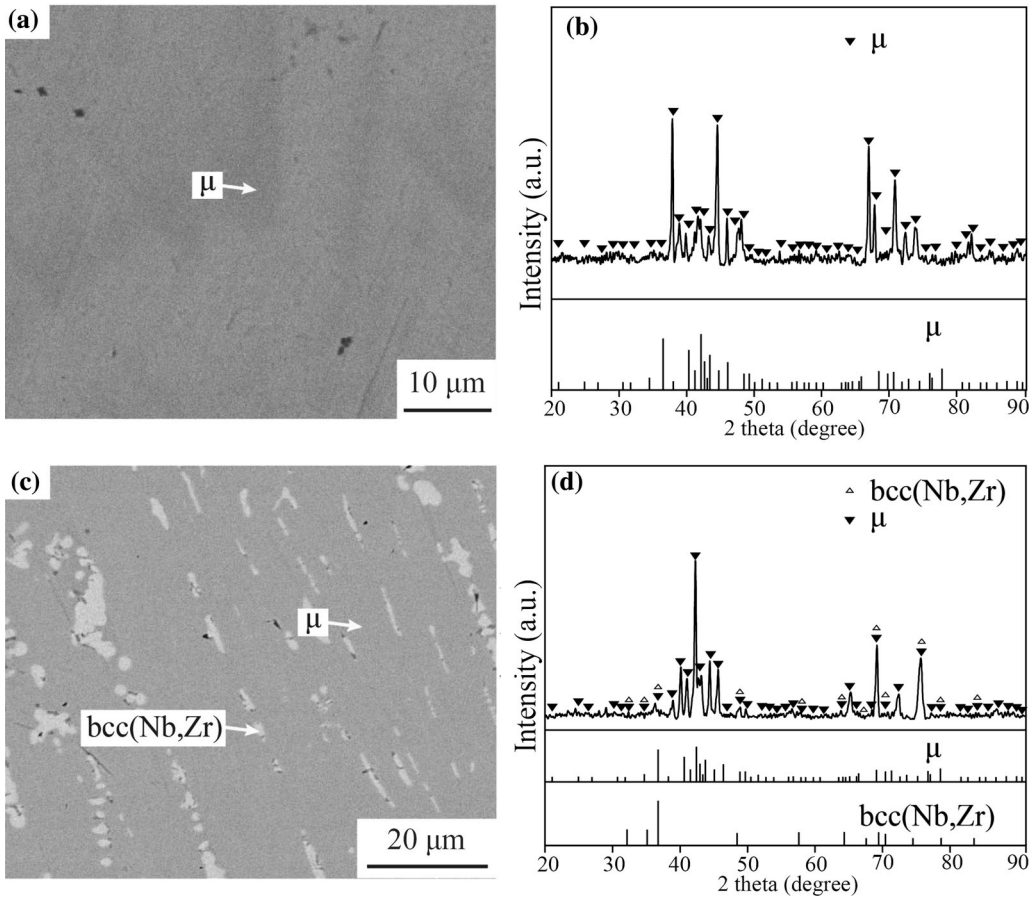

Fig. 6—BSE micrographs and XRD patterns of as-cast alloys: (*a*) and (*b*) a35; (*c*) and (*d*) a36.

μ and CoZr were observed. μ was first precipitated from the liquid phase. Additionally, the liquid phase moved to the monovariant line of liq. $\rightarrow$ CoZr + μ, then the liquid composition was at the invariant transformation point liq. $\rightarrow$ CoZr + λ_2 + μ. From the microstructure of alloy a35, single phase μ was observed as shown in Figure 6(a). It was further verified that only μ existed by the XRD pattern in Figure 6(b). So, the solidification path can be conjectured: liq. $\rightarrow$ μ. The black and white phases were μ and bcc(Nb, Zr) based on the analyses of the EDS and XRD patterns of alloy a36 in Figures 6(c) and (d). μ was first precipitated, then the liquid phase moved to the univariant line of liq. $\rightarrow$ bcc(Nb, Zr) + μ. The microstructure and XRD patterns of alloy a40 are exhibited in Figures 7(a) and (b). $CoZr_2$ was solidified from the liquid phase, then the liquid composition was at the univariant line and transformed into bcc(Nb, Zr) + $CoZr_2$ microstructure.

There were bcc(Nb, Zr), CoZr, and $CoZr_2$ from the microstructure and XRD patterns of alloy a45, as shown in Figures 7(c) and (d). bcc(Nb, Zr) was first precipitated, and the liquid phase was at the monovariant line and transformed into bcc(Nb, Zr) + CoZr microstructure. However, the content of CoZr was minimal. Thus, the eutectic structure bcc(Nb, Zr) + CoZr loses the characterization of typical eutectic microstructure. Finally, the remaining liquid decomposed the ternary eutectic microstructure bcc(Nb, Zr) + CoZr + $CoZr_2$. The microstructure and XRD patterns of alloy a46 are demonstrated in Figures 7(e) and (f), where bcc(Nb, Zr) and μ were observed. bcc(Nb, Zr) was first precipitated and the liquid composition was at the univariant line and transformed into bcc(Nb, Zr) + μ microstructure.

B. *Isothermal Section at 1100 °C*

Twenty-four annealed specimens were analyzed using SEM/EDS and XRD patterns to construct the phase relationships of 1100 °C. The constituent phases and compositions are outlined in Table III.

On the Co-rich side, the two-phase microstructures, fcc(Co) + λ_2 in alloy b3 and $Co_{23}Zr_6$ + λ_2 in alloy b8, and a three-phase microstructure fcc(Co) + $Co_{23}Zr_6$ + λ_2 in alloy b5 were observed, as shown in Figure 8. The microstructure and XRD patterns of alloy b12 are displayed in Figures 9(a) and (b), where λ_2 and μ were observed. A three-phase equilibrium CoZr + λ_2 + μ was measured because of the microstructure and XRD patterns of alloy b14 in Figures 9(c) and (d).

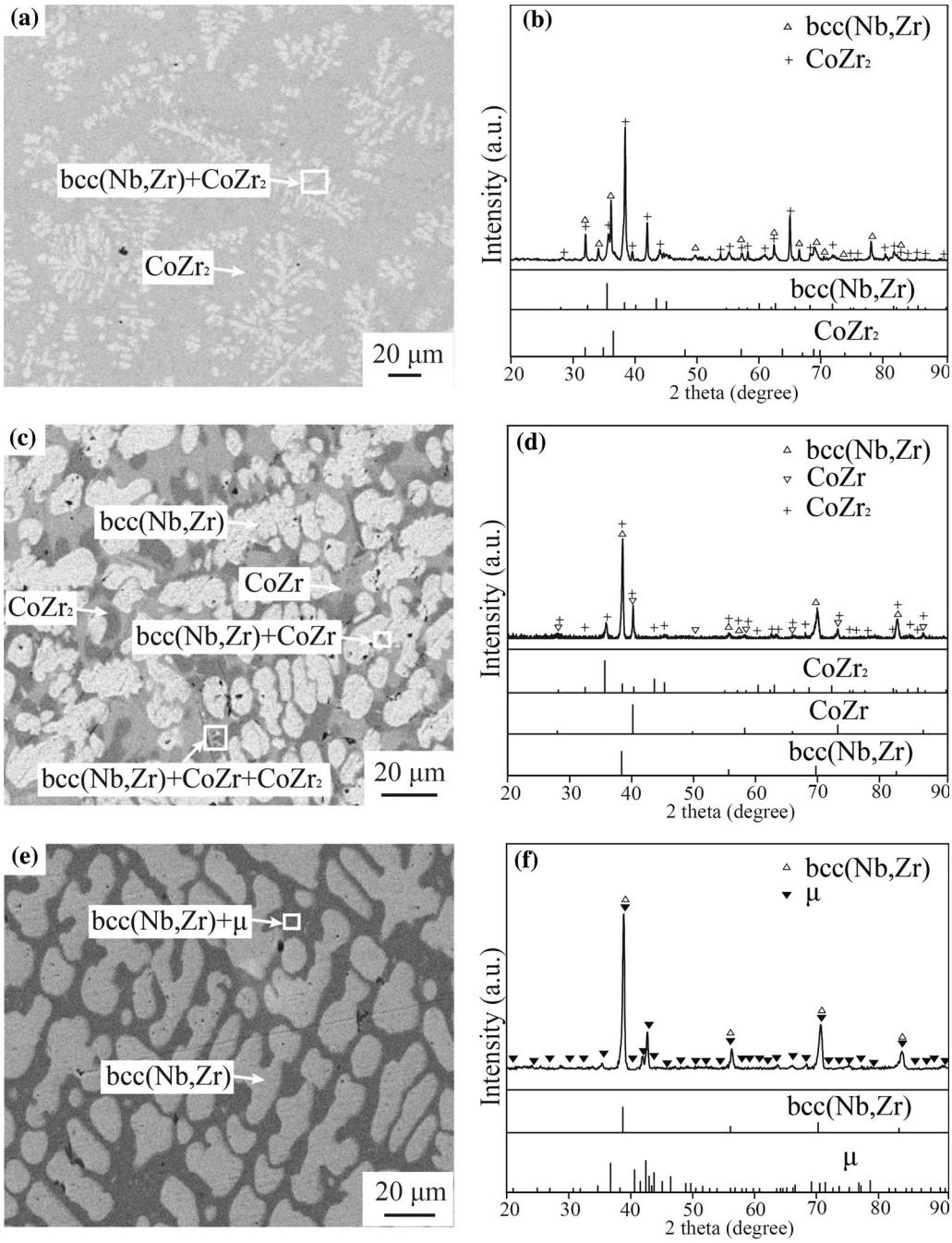

Fig. 7—BSE micrographs and XRD patterns of as-cast alloys: (*a*) and (*b*) a40; (*c*) and (*d*) a45; (*e*) and (*f*) a46.

Additionally, the measured maximum solubilities of Nb in $Co_{23}Zr_6$ and CoZr were ~ 3.1 and ~ 11.9 at. pct, and the maximum solubility of Zr in μ was ~ 17.9 at. pct. The microstructures and XRD patterns of alloys b15 and b16 are demonstrated in Figures 9(e) and (f) and Figures 10(a) and (b), where two two-phase microstructures, CoZr + μ and bcc(Nb, Zr) + μ, were observed.

The phase related to liquid can be observed based on the phase constituents of alloys b20, b21, and b22. The phase equilibria, CoZr + liquid, bcc(Nb, Zr) + CoZr + liquid, and bcc(Nb, Zr) + liquid, were determined following the microstructures of Figures 10(c) and (d) and 11. Furthermore, a three-phase equilibrium bcc(Nb, Zr) + liquid + μ can be deduced according to the analyses of alloys b15 and b16.

According to the experimental results, the phase relationships of Co–Nb–Zr system were confirmed. Co_2Nb and Co_2Zr with the same C15 structure formed a continuous compound from Co_2Nb to Co_2Zr at 1100 °C. Three three-phase equilibria, fcc(Co) + $Co_{23}Zr_6$ + λ_2, CoZr + λ_2 + μ, and bcc(Nb, Zr) + CoZr + liquid, were obtained, and a three-phase region bcc(Nb, Zr) + CoZr + μ was deduced. Moreso, the maximum solubilities of Nb in $Co_{23}Zr_6$ and

Table III. Constituent Phases and Compositions of the Co–Nb–Zr Equilibrated Alloys Annealed at 1100 °C

No.	Measured Alloy Compositions (at. Pct)			Equilibrated Phases	Phase compositions (At. Pct)		
	Co	Nb	Zr		Co	Nb	Zr
b1	85.4	13.9	0.7	fcc(Co)	96.3	3.3	0.4
				λ_2	74.0	25.3	0.7
b2	84.2	10.6	5.2	fcc(Co)	96.4	3.0	0.6
				λ_2	77.1	15.3	7.6
b3	84.2	9.9	5.9	fcc(Co)	97.5	2.1	0.4
				λ_2	75.1	15.0	9.9
b4	84.1	8.9	7.0	fcc(Co)	97.4	1.8	0.8
				λ_2	75.4	13.1	11.5
b5	85.7	4.8	9.5	fcc(Co)	97.0	1.7	1.3
				$Co_{23}Zr_6$	79.5	3.1	17.4
				λ_2	75.2	10.3	14.5
b6	77.0	5.2	17.8	$Co_{23}Zr_6$	79.0	2.3	18.7
				λ_2	74.2	9.3	16.5
b7	76.3	4.8	18.9	$Co_{23}Zr_6$	79.2	1.6	19.2
				λ_2	73.8	7.3	18.9
b8	76.1	4.1	19.8	$Co_{23}Zr_6$	79.1	1.1	19.8
				λ_2	72.9	7.0	20.1
b9	75.7	3.4	20.9	$Co_{23}Zr_6$	78.8	0.6	20.6
				λ_2	72.2	6.5	21.3
b10	59.1	39.7	1.2	λ_2	65.3	33.1	11.6
				μ	51.2	48.1	0.7
b11	57.4	36.5	6.1	λ_2	66.3	24.6	9.1
				μ	49.2	46.6	4.2
b12	58.2	31.9	9.9	λ_2	65.9	20.1	14.0
				μ	50.8	43.0	6.2
b13	57.6	28.6	13.8	λ_2	65.5	14.9	19.6
				μ	49.1	43.5	7.4
b14	57.2	12.8	30.0	CoZr	50.3	11.9	37.8
				λ_2	66.2	7.1	26.7
				μ	51.7	30.4	17.9
b15	49.2	25.5	25.3	CoZr	49.9	10.9	39.2
				μ	48.9	33.3	17.8
b16	29.6	67.7	2.7	bcc(Nb,Zr)	2.4	96.7	9.8
				μ	44.5	52.3	3.2
b17	28.3	66.8	4.9	bcc(Nb,Zr)	1.8	96.3	1.9
				μ	46.9	44.6	8.5
b18	41.8	3.8	54.4	CoZr	48.9	2.6	48.5
				liquid	35.7	3.1	61.2
b19	40.4	8.0	51.6	CoZr	49.7	3.5	46.8
				liquid	34.5	11.4	54.1
b20	41.1	11.0	47.9	CoZr	48.4	7.6	44.0
				liquid	34.7	13.9	51.4
b21	34.2	30.9	34.9	bcc(Nb,Zr)	1.7	92.1	6.2
				CoZr	48.9	11.1	40.0
				liquid	33.1	21.3	45.6
b22	19.6	34.8	45.6	bcc(Nb,Zr)	1.7	54.0	44.3
				liquid	28.7	23.7	47.6
b23	12.9	29.7	57.4	bcc(Nb,Zr)	0.8	42.9	56.3
				liquid	24.4	18.9	56.7
b24	10.7	10.0	79.3	bcc(Nb,Zr)	1.2	13.7	85.1
				liquid	22.8	3.7	73.5

CoZr were ~ 3.1 at. pct and ~ 11.9 at. pct, and the maximum solubility of Zr in μ was ~ 17.9 at. pct.

C. *Isothermal Section at 1000 °C*

The experimental information of twenty-three samples annealed at 1000 °C is listed in Table IV. The analyses of several samples for three-phase equilibria are discussed as follows.

Three three-phase equilibria, fcc(Co) + $Co_{23}Zr_6$ + λ_2 in alloy c5, CoZr + λ_2 + μ in alloy c13, and bcc(Nb, Zr) + CoZr + μ in alloy c16, were determined based on the microstructures and XRD patterns as shown in Figure 12. The microstructures and XRD

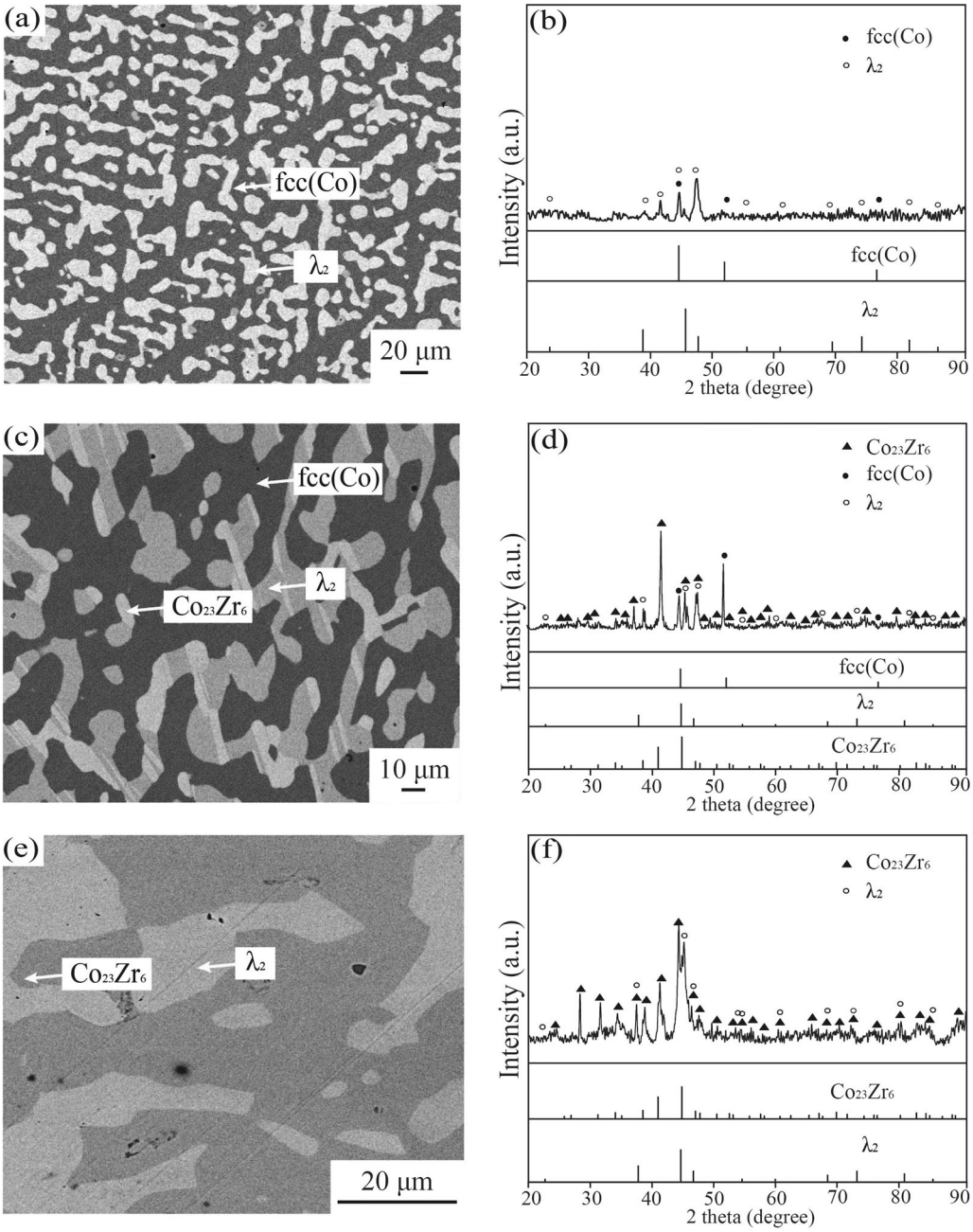

Fig. 8—BSE micrographs and XRD patterns of alloys annealed at 1100 °C: (*a*) and (*b*) b3; (*c*) and (*d*) b5; (*e*) and (*f*) b8.

patterns of alloys c17 and c18 are presented in Figure 13, where the three-phase microstructures, bcc(Nb, Zr) + CoZr + $CoZr_2$ and bcc(Nb, Zr) + $CoZr_2$ + liquid, were determined. According to the experimental data above, the maximum solubilities of Nb in $Co_{23}Zr_6$, CoZr, and $CoZr_2$ were ~ 2.8, ~ 11.3, and ~ 8.7 at. pct, and the maximum solubility of Zr in μ was ~ 17.5 at. pct, respectively.

Furthermore, typical diffusion layers of λ_2 and μ were observed by the Nb80Zr20/Co diffusion couple annealed at 1000 °C as shown in Figure 14. Due to the presence of CoZr, a three-phase conjunction corresponding to bcc(Nb, Zr) + CoZr + μ was identified in Figure 14. The compositions of equilibrium phases of Nb80Zr20/Co diffusion couple obtained using EPMA at 1000 °C are shown in Table V, and tie lines are shown using the dashed lines with inverted triangles in Figure 15(b). Furthermore, the phase relationships and phase compositions obtained by the diffusion couple were almost identical to those of the equilibrated alloys, as shown in Figure 15(b).

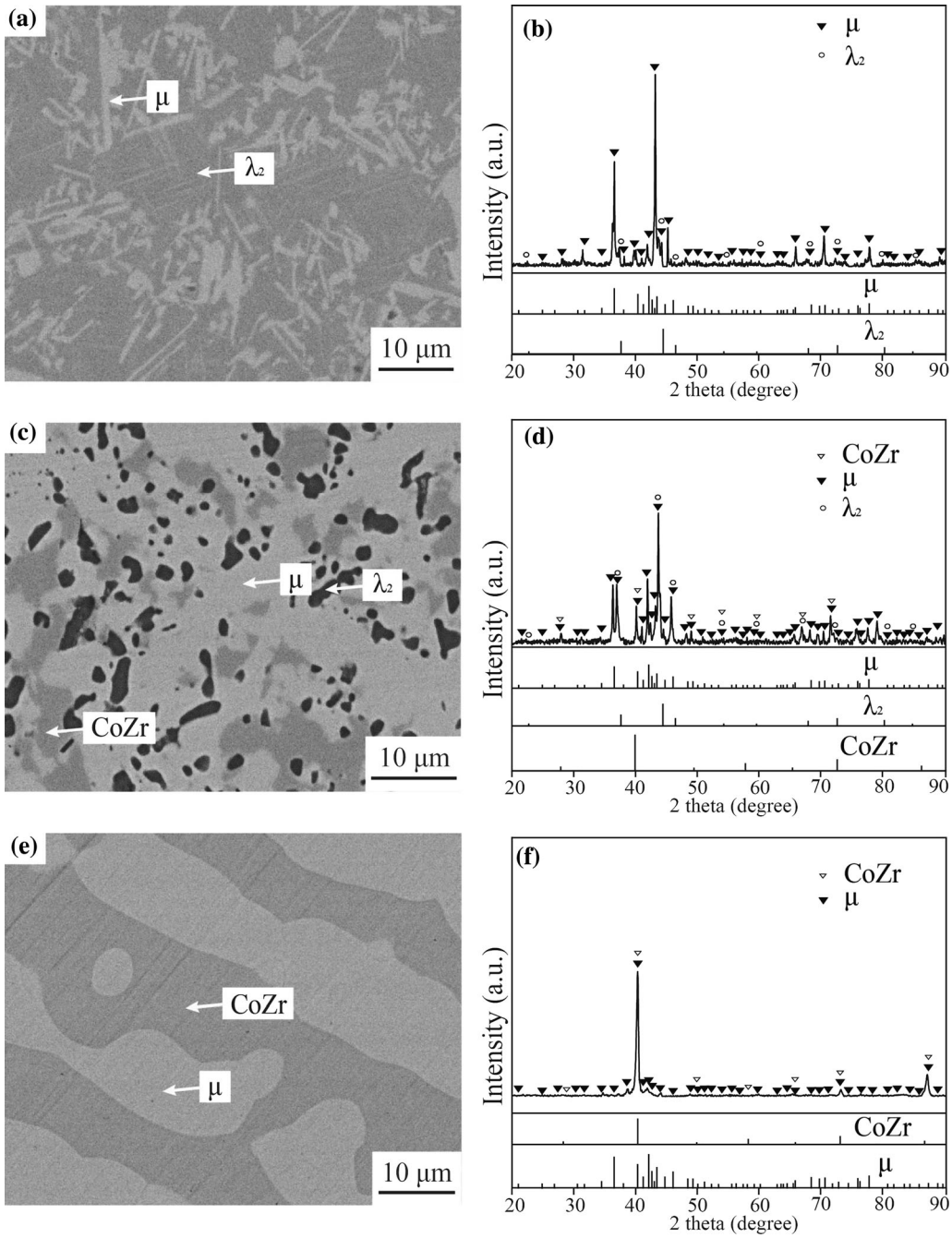

Fig. 9—BSE micrographs and XRD patterns of alloys annealed at 1100 °C: (*a*) and (*b*) b12; (*c*) and (*d*) b14; (*e*) and (*f*) b15.

V. THERMODYNAMIC MODELING

A. *Thermodynamic Model*

The Gibbs energy functions for the unary phases of the pure elements Co, Nb, and Zr were taken from the SGTE database.[31]

The Gibbs energies of solution phases (liquid, bcc fcc, and hcp) in the Co–Nb–Zr system are expressed:

$$G_{\mathrm{m}}^{\phi}(T) = x_{\mathrm{Co}} G_{\mathrm{Co}}^{\phi}(T) + x_{\mathrm{Nb}} G_{\mathrm{Nb}}^{\phi}(T) + x_{\mathrm{Zr}} G_{\mathrm{Zr}}^{\phi}(T) + \mathrm{R}T(x_{\mathrm{Co}} \ln(x_{\mathrm{Co}}) + x_{\mathrm{Nb}} \ln(x_{\mathrm{Nb}}) + x_{\mathrm{Zr}} \ln(x_{\mathrm{Zr}})) + {}^{\mathrm{E}}G_{\mathrm{m}}^{\phi} + {}^{mg}G_{\mathrm{m}}^{\phi} \quad [1]$$

where x_{Co}, x_{Nb}, and x_{Zr} indicate the molar fractions of the pure elements Co, Nb, and Zr, respectively. ${}^{\mathrm{E}}G_{\mathrm{m}}^{\phi}$ is the molar excess Gibbs energy, and its Redlich–Kister polynomial function can be described[32]:

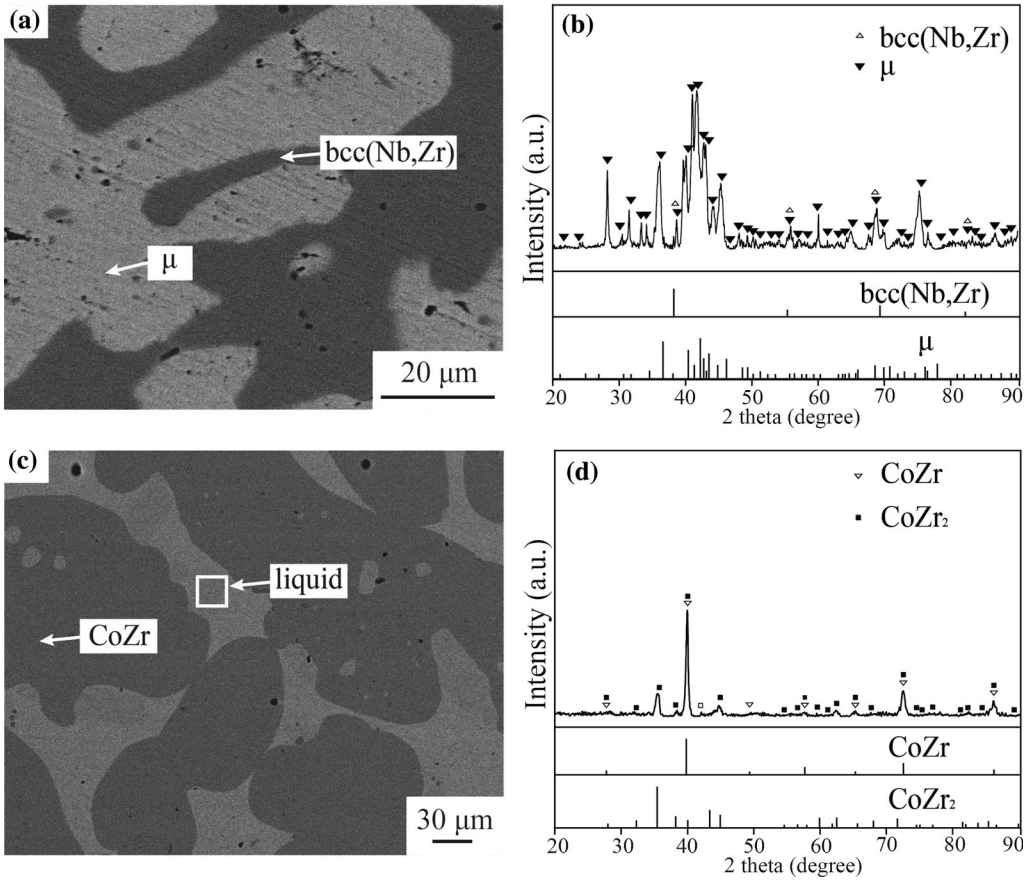

Fig. 10—BSE micrographs and XRD patterns of alloys annealed at 1100 °C: (*a*) and (*b*) b18; (*c*) and (*d*) b19.

$$
\begin{aligned}
{}^{E}G_{m}^{\phi}(T) = {} & x_{Co}x_{Nb}\sum_{j}{}^{j}L_{Co,Nb}^{\phi}(x_{Co}-x_{Nb})^{j} \\
& + x_{Co}x_{Zr}\sum_{j}{}^{j}L_{Co,Zr}^{\phi}(x_{Co}-x_{Zr})^{j} \\
& + x_{Nb}x_{Zr}\sum_{j}{}^{j}L_{Nb,Zr}^{\phi}(x_{Nb}-x_{Zr})^{j} \\
& + x_{Co}x_{Nb}x_{Zr}L_{Co,Nb,Zr}^{\phi}
\end{aligned}
\qquad [2]
$$

in which ${}^{j}L_{Co,Nb}^{\phi}$, ${}^{j}L_{Co,Zr}^{\phi}$, and ${}^{j}L_{Nb,Zr}^{\phi}$ are the interaction parameters obtained from Co–Nb,[19] Co–Zr,[27] and Nb–Zr[29] systems. $L_{Co,Nb,Zr}^{\phi}$ is the ternary interaction parameters and expressed as follows:

$$
\begin{aligned}
L_{Co,Nb,Zr}^{\phi} = {} & x_{Co}{}^{0}L_{Co,Nb,Zr}^{\phi} + x_{Nb}{}^{1}L_{Co,Nb,Zr}^{\phi} \\
& + x_{Zr}{}^{2}L_{Co,Nb,Zr}^{\phi}
\end{aligned}
\qquad [3]
$$

where ${}^{j}L_{Co,Nb,Zr}^{\phi} = a_j + b_j T$ ($j = 0$, 1, and 2). The factors of a_j and b_j were required to be optimized in this work.

CoZr with B2 structure is described as an ordered phase of bcc_A2 and modeled as (Co, Nb, Zr, Va)$_{0.5}$(Co, Nb, Zr, Va)$_{0.5}$(Va)$_3$. The Gibbs energy function of CoZr can be constructed:

$$
G_{m}^{CoZr} = G_{m}^{dis}(x_i) + G_{m}^{ord}(y_i', y_i'') - G_{m}^{ord}(x_i) \qquad [4]
$$

where $G_{m}{}^{dis}(x_i)$ denotes the Gibbs energy of bcc_A2. $G_{m}^{ord}(y_i', y_i'') - G_{m}^{ord}(x_i)$ means the ordered contribution to Gibbs energy.

The intermediate compounds $Co_{11}Zr_2$, $Co_{23}Zr_6$, $CoZr_2$, Co_7Nb_2, λ_1, λ_2 and λ_3 are modeled as $(Co)_{11}(Nb,Zr)_2$, $(Co)_{23}(Nb,Zr)_6$, $(Co,Zr)(Nb,Zr)_2$, Co_7Nb_2, $(Co,Nb)_2(Co,Nb)$, $(Co,Nb,Zr)_2(Co,Nb,Zr)$ and $(Co,Nb)_2(Co,Nb)$, respectively. $CoZr_3$ and μ are described as $(Co,Zr)(Co,Zr)Zr_2$ and $(Co,Nb,Zr)_1(Nb,Zr)_4(Co,Nb,Zr)_2(Co,Nb,Zr)_6$. Taking Laves phase λ_2 as an example, the Gibbs energy function is expressed:

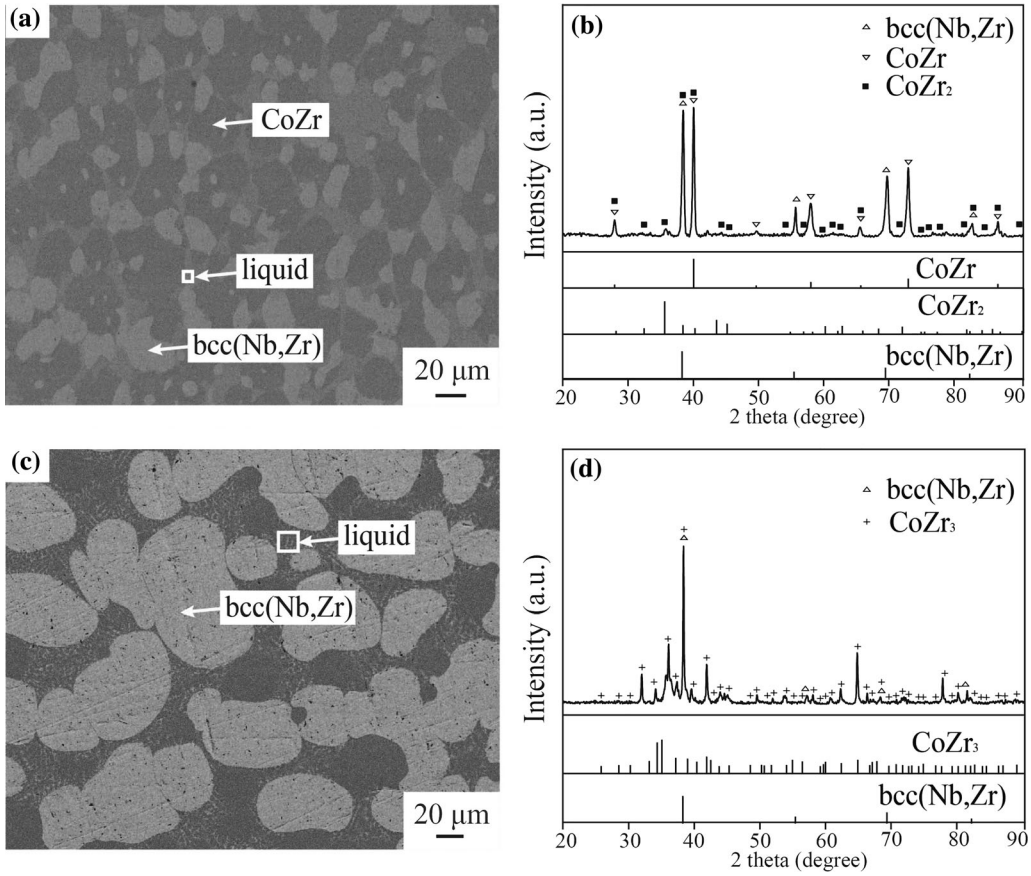

Fig. 11—BSE micrographs and XRD patterns of alloys annealed at 1100 °C: (*a*) and (*b*) b21; (*c*) and (*d*) b22.

$$
\begin{aligned}
G_{\mathrm{m}}^{\lambda_2} = {} & y'_{\mathrm{Co}}\left(y_{\mathrm{Co}}{}''G_{\mathrm{Co:Co}}^{\lambda_2} + y''_{\mathrm{Nb}}G_{\mathrm{Co:Nb}}^{\lambda_2} + y''_{\mathrm{Zr}}G_{\mathrm{Co:Zr}}^{\lambda_2}\right) \\
& + y'_{\mathrm{Nb}}\left(y''_{\mathrm{Co}}G_{\mathrm{Nb:Co}}^{\lambda_2} + y''_{\mathrm{Nb}}G_{\mathrm{Nb:Nb}}^{\lambda_2} + y''_{\mathrm{Zr}}G_{\mathrm{Nb:Zr}}^{\lambda_2}\right) \\
& + y'_{\mathrm{Zr}}\left(y''_{\mathrm{Co}}G_{\mathrm{Zr:Co}}^{\lambda_2} + y''_{\mathrm{Nb}}G_{\mathrm{Zr:Nb}}^{\lambda_2} + y''_{\mathrm{Zr}}G_{\mathrm{Zr:Zr}}^{\lambda_2}\right) \\
& + 2\mathrm{R}T\left(y'_{\mathrm{Co}}\ln(y'_{\mathrm{Co}}) + y'_{\mathrm{Nb}}\ln(y'_{\mathrm{Nb}}) + y'_{\mathrm{Zr}}\ln(y'_{\mathrm{Zr}})\right) \\
& + \mathrm{R}T\left(y''_{\mathrm{Co}}(y''_{\mathrm{Co}}) + y''_{\mathrm{Nb}}\ln(y''_{\mathrm{Nb}}) + y''_{\mathrm{Zr}}\ln(y''_{\mathrm{Zr}})\right) + {}^{\mathrm{E}}G_{\mathrm{m}}^{\lambda_2}
\end{aligned}
\quad [5]
$$

where y'_* and y''_* are the fractions of sites of elements (* = Co, Nb, and Zr) on the first and second sublattices. ${}^{\mathrm{E}}G_{\mathrm{m}}^{\lambda_2}$ is the excess Gibbs energy.

B. *Assessment Procedure*

The thermodynamic parameters of Co–Nb and Nb–Zr systems were taken from the literatures[19] and[29] in the Co–Nb–Zr system. To unify the thermodynamic parameters of phases with the same crystal structure in the Co-based superalloys thermodynamic database, the thermodynamic parameters of λ_2 in the Co–Zr system[27] were slightly modified according to the corresponding thermodynamic parameters in the Co–Nb system.[29] Furthermore, the Co–Nb–Zr system was optimized using the PARROT module in Thermo-Calc software and the PanOptimizer module in Pandat software to comply with the experimental data of the current work.

C. *Thermodynamic Modeling*

Thermodynamic models and obtained thermodynamic parameters of each phase in the Co–Nb–Zr system are shown in Table VI. The calculated phase relationships at 1100 °C and 1000 °C in comparison with the experimental information are shown in Figures 15(a) and (b). Three three-phase equilibria, fcc(Co) + $Co_{23}Zr_6$ + λ_2, CoZr + λ_2 + μ and bcc(Nb,Zr) + CoZr + liquid, at the 1100 °C and five

Table IV. Constituent Phases and Compositions of the Co–Nb–Zr Equilibrated Alloys Annealed at 1000 °C

	Measured Alloy Compositions (At. Pct)				Phase Compositions (At. Pct)		
No.	Co	Nb	Zr	Equilibrated Phases	Co	Nb	Zr
c1	84.8	12.7	2.5	fcc(Co)	97.9	2.0	0.1
				λ_2	74.8	20.8	4.4
c2	83.4	11.1	5.5	fcc(Co)	98.6	1.4	0.0
				λ_2	75.0	16.7	8.3
c3	85.8	8.7	5.5	fcc(Co)	97.9	1.5	0.6
				λ_2	75.7	14.2	10.1
c4	82.3	9.2	8.5	fcc(Co)	99.0	0.6	0.4
				λ_2	75.4	12.8	11.8
c5	83.5	5.0	11.5	fcc(Co)	97.4	1.3	1.3
				$Co_{23}Zr_6$	79.4	2.8	17.9
				λ_2	75.3	9.7	15.0
c6	76.7	4.6	18.7	$Co_{23}Zr_6$	79.1	1.9	19.0
				λ_2	73.3	8.6	18.1
c7	75.8	3.9	20.3	$Co_{23}Zr_6$	78.8	1.2	20.0
				λ_2	73.7	5.7	20.6
c8	75.5	2.0	22.5	$Co_{23}Zr_6$	78.9	0.4	20.7
				λ_2	72.3	3.6	24.1
c9	56.5	41.2	2.3	λ_2	63.5	33.3	3.2
				μ	49.8	48.4	1.8
c10	56.8	35.7	7.5	λ_2	66.0	21.8	12.2
				μ	49.1	47.4	3.5
c11	57.5	29.8	12.7	λ_2	65.3	19.0	15.7
				μ	52.3	37.8	9.9
c12	58.1	24.5	17.4	λ_2	66.1	12.0	21.9
				μ	51.5	32.8	15.7
c13	56.0	14.2	29.8	CoZr	50.5	11.3	38.2
				λ_2	65.9	7.5	26.6
				μ	51.7	30.8	17.5
c14	30.2	67.1	2.7	bcc(Nb,Zr)	3.6	95.3	0.1
				μ	45.2	51.4	3.4
c15	29.6	66.2	4.2	bcc(Nb,Zr)	2.1	96.6	1.3
				μ	44.2	49.5	6.3
c16	40.7	32.9	26.4	bcc(Nb,Zr)	6.2	89.8	4.0
				COZr	49.4	12.8	37.8
				μ	46.3	38.4	15.3
c17	34.2	20.7	45.1	CoZr	49.1	8.5	42.4
				$CoZr_2$	34.1	8.3	57.6
				μ	1.1	92.2	6.7
c18	24.5	24.0	51.5	bcc(Nb,Zr)	0.9	83.0	16.1
				$CoZr_2$	31.9	8.7	59.4
				liquid	25.6	15.3	59.1
c19	40.4	5.6	54.0	CoZr	48.7	2.6	48.7
				$CoZr_2$	32.1	8.1	59.8
c20	40.3	4.7	55.0	CoZr	48.9	2.0	49.1
				$CoZr_2$	32.0	6.9	61.1
c21	40.6	2.2	57.2	CoZr	49.3	0.7	50.0
				$CoZr_2$	33.5	3.7	62.8
c22	12.4	16.2	71.4	bcc(Nb,Zr)	2.0	21.4	76.6
				liquid	22.7	11.7	65.6
c23	16.6	3.9	79.5	bcc(Nb,Zr)	2.3	9.3	88.4
				liquid	23.6	1.9	74.5

three-phase regions, fcc(Co) + $Co_{23}Zr_6$ + λ_2, CoZr + λ_2 + μ, bcc(Nb,Zr) + $CoZr_2$ + liquid, bcc(Nb,Zr) + CoZr + $CoZr_2$ and bcc(Nb,Zr) + CoZr + μ at 1000 °C were well reproduced in the calculated isothermal sections.

The comparison of the calculated primary solidification region with the experimental data of the Co–Nb–Zr system is shown in Figure 16(a), in which ten primary solidification regions, fcc(Co), bcc(Nb, Zr), $Co_{11}Zr_2$, $Co_{23}Zr_6$, CoZr, $CoZr_2$, λ_1, λ_2, λ_3, and μ in the liquidus

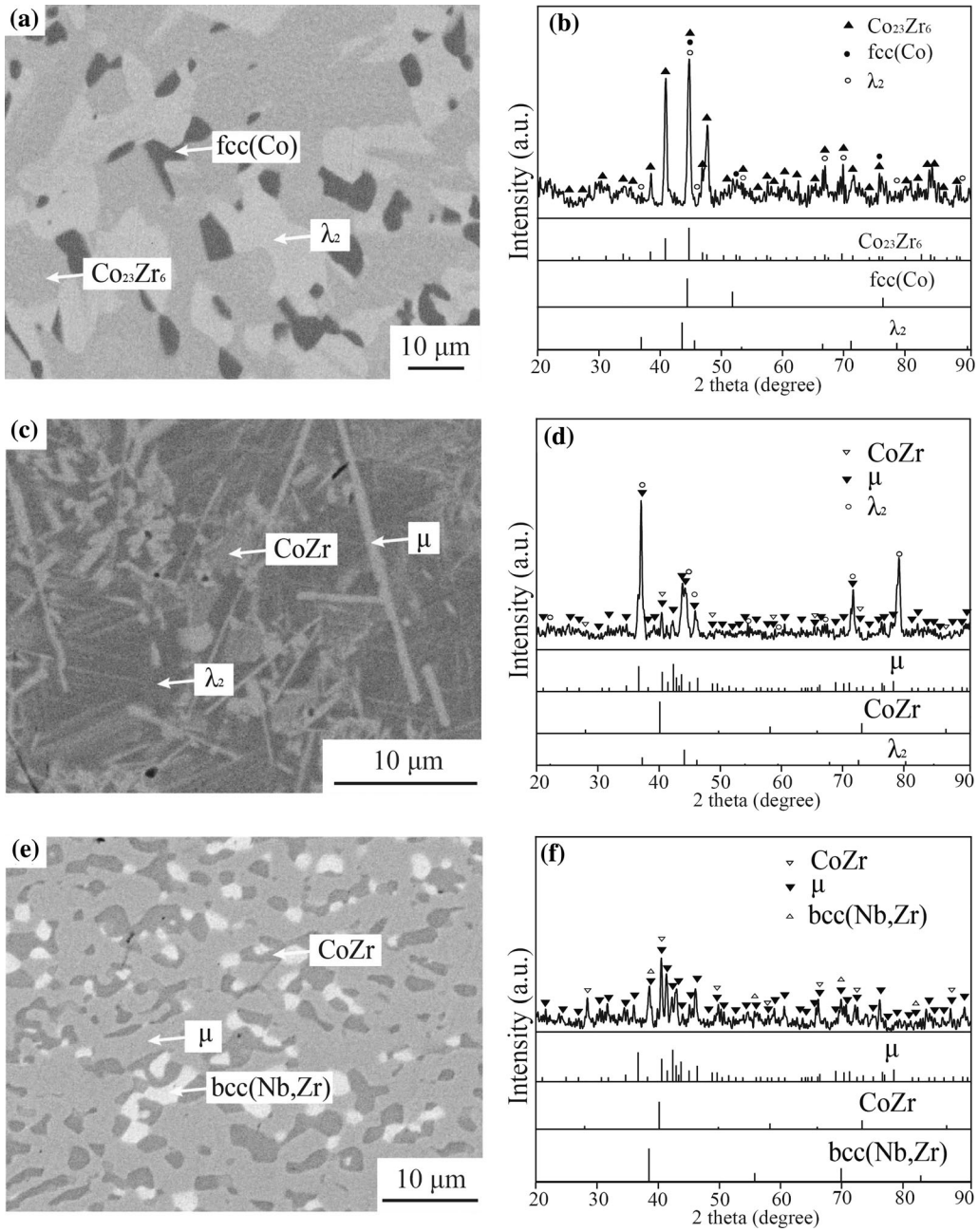

Fig. 12—BSE micrographs and XRD patterns of alloys annealed at 1000 °C: (*a*) and (*b*) c5; (*c*) and (*d*) c13; (*e*) and (*f*) c16.

surface projection were very well reproduced. The calculated liquidus surface projection with isotherms is exhibited in Figure 16(b), in which seven invariant reactions: liq. $\rightarrow$ CoZr + λ_2 + μ, liq. $\rightarrow$ $Co_{23}Zr_6$ + fcc(Co) + λ_2, liq. $\rightarrow$ $Co_{11}Zr_2$ + $Co_{23}Zr_6$ + fcc(Co), liq. $\rightarrow$ fcc(Co) + λ_2 + λ_3, liq. + $\mu \rightarrow$ bcc(Nb, Zr) + CoZr, liq. + $\lambda_2 \rightarrow \lambda_1$ + μ, liq. $\rightarrow$ bcc(Nb, Zr) + CoZr + $CoZr_2$, and six maximum points, Max1, Max2, Max3, Max4, Max5 and Max6 on the monovariant lines were manifested.

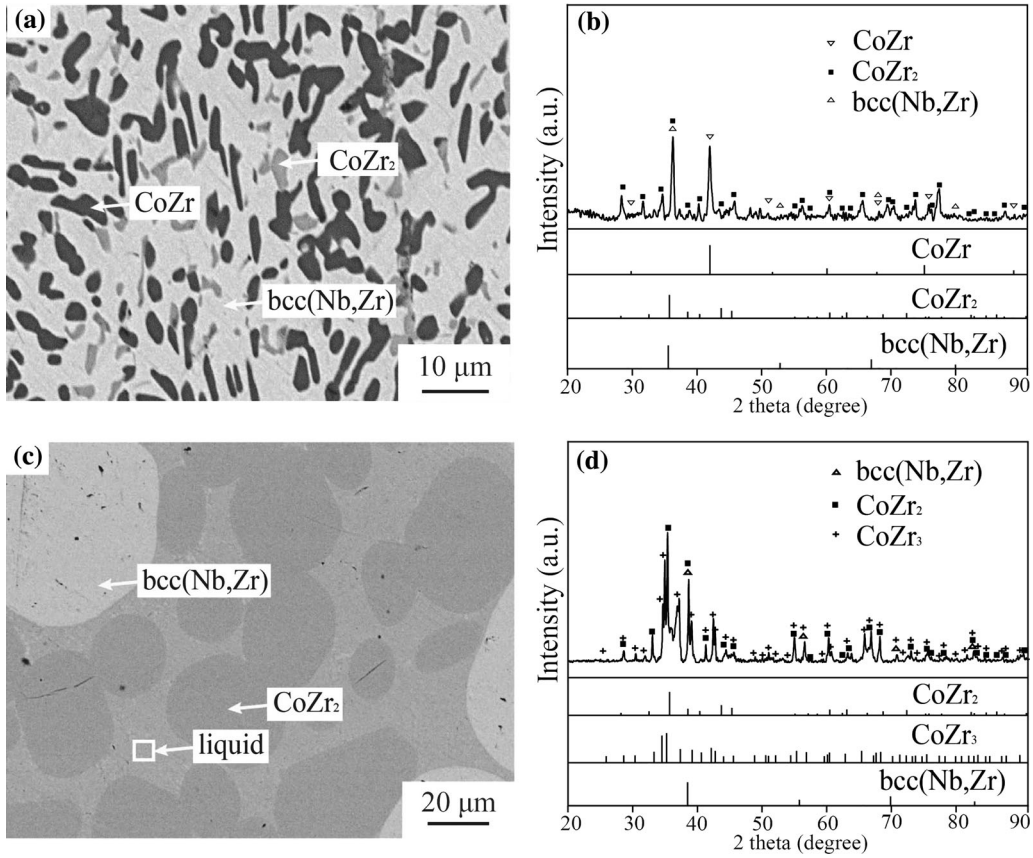

Fig. 13—BSE micrographs and XRD patterns of alloys annealed at 1000 °C: (*a*) and (*b*) b17; (*c*) and (*d*) b18.

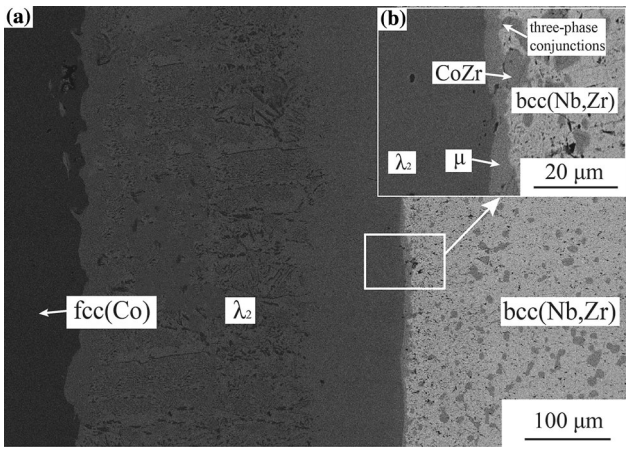

Fig. 14—(*a*) BSE micrograph of the Nb80Zr20/Co diffusion couple annealed at 1000 °C for 360 h; (*b*) enlarged section.

Table V. Tie-Lines Determined from the Nb80Zr20/Co Diffusion Couple Annealed at 1000 °C

Equilibria Phases		Phase Compositions (At. Pct)					
		Phase 1			Phase 2		
No.	Phase 1/Phase 2	Co	Nb	Zr	Co	Nb	Zr
1	fcc(Co)/λ_2	96.8	2.6	0.6	75.4	18.4	6.2
2	λ_2/μ	66.3	14.6	19.1	51.9	34.3	13.8
3	CoZr/μ	48.8	13.3	37.9	46.6	38.7	14.7
4	bcc(Nb,Zr)/μ	1.6	95.8	2.6	46.6	38.7	14.7
5	bcc(Nb,Zr)/CoZr	1.6	95.8	2.6	48.8	13.3	37.9

The calculated solidification path by the Scheil model[33] was compared with those of alloys a35 and a45 in experiments to further verify the reliability of the calculated liquidus surface projection. It was found that only single-phase μ was observed from alloy a35, as shown in Figures 6(a) and (b). The solidification paths obtained by the Scheil model were as follows liq. $\rightarrow \mu$ and liq. $\rightarrow$ bcc(Nb, Zr) + μ. When a eutectic microstructure bcc(Nb, Zr) + μ was precipitated, the contents of the remaining liquid phase was 5.5 at. pct using the Scheil model. Therefore, it was challenging to analyze EDS and XRD patterns. In addition, the calculated solidification path using the Lever model was liq. $\rightarrow \mu$. So, the calculated results were acceptable.

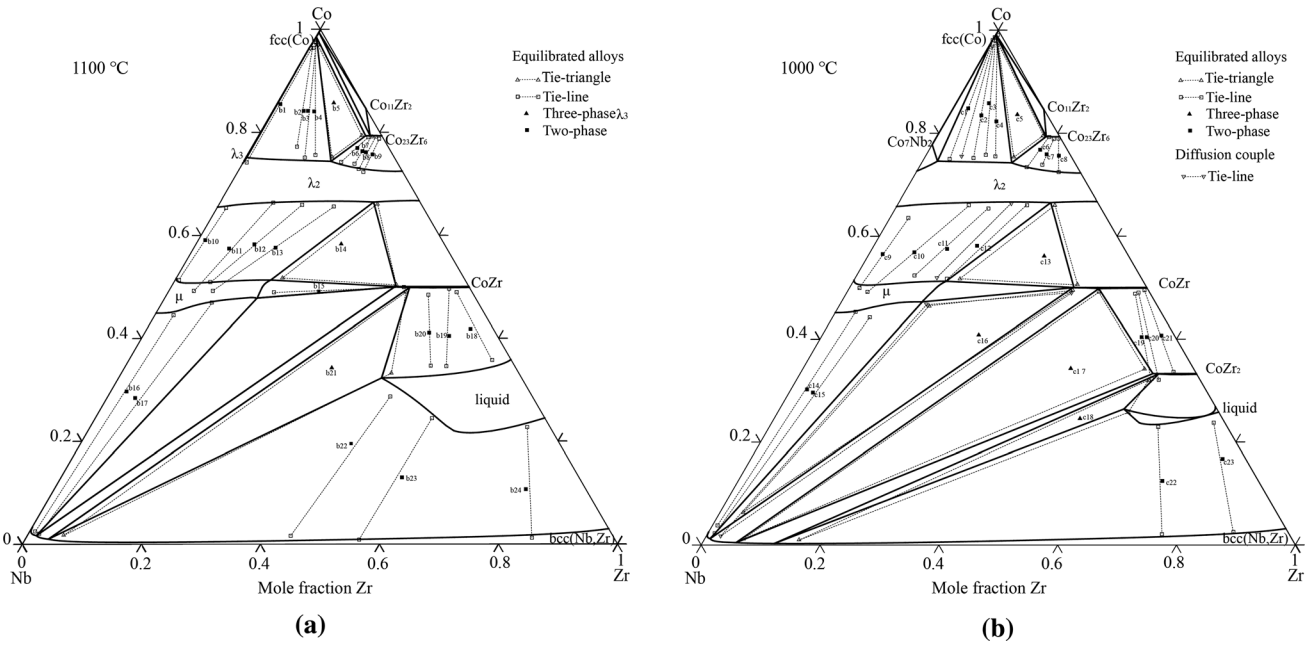

Fig. 15—Calculated isothermal sections of the Co–Nb–Zr system in comparison with the experimental data: (*a*) 1100 °C; (*b*) 1000 °C.

There were only three phases, bcc(Nb, Zr), CoZr, and $CoZr_2$, as shown in Figures 7(c) and (d), based on the analyses of the microstructure and XRD pattern of alloy a45. The solidification path of alloy a45 can be inferred: liq. → bcc(Nb,Zr), liq. → bcc(Nb,Zr) + CoZr and liq. → bcc(Nb, Zr) + CoZr + $CoZr_2$, which was the same as the calculation of the solidification path by the Scheil model. Furthermore, the invariant reaction scheme related to liquid and the invariant reactions are exhibited in Figure 17 and Table VII.

VI. CONCLUSIONS

The experimental liquidus surface projection of the Co–Nb–Zr system was constructed by analyses of solidification paths of as-cast alloys, where ten primary solidification regions and seven invariant reactions were obtained, respectively.

The experimental isothermal sections of the Co–Nb–Zr system at 1100 and 1000 °C were constructed. Three three-phase regions at 1100 °C and five three-phase regions at 1000 °C were also determined. Notably, Co_2Nb and Co_2Zr with the same C15 structure formed a continuous compound from Co_2Nb to Co_2Zr at 1100 and 1000 °C. The maximum solubilities of Nb in $Co_{23}Zr_6$ and CoZr were ~ 3.1 and ~ 11.9 at. pct at 1100 °C, and the maximum solubilities of Nb in $Co_{23}Zr_6$, CoZr and $CoZr_2$ were ~ 2.8, ~ 11.3 and ~ 8.7 at. pct at 1000 °C. The maximum solubility of Zr in μ was ~ 17.9 at 1100 °C and ~ 17.5 at. pct at 1000 °C.

A thermodynamic description of the Co–Nb–Zr system was established using the CALPHAD method according to the experimental data of the current work. Furthermore, a set of reasonable thermodynamic parameters of the Co–Nb–Zr system was obtained, which can provide theoretical guidance for the composition design of Co-based superalloys.

Table VI. Optimized Thermodynamic Parameters and Thermodynamic Models of Individual Phases in the Co–Nb–Zr System

Phase	Thermodynamic Model and Parameter	References
Liquid	$(Co,Nb,Zr)_1$	
	${}^0L^{liquid}_{Co,Nb} = -90304.0 + 4.379T$	[19]
	${}^1L^{liquid}_{Co,Nb} = -45916.6 + 20.647T$	[19]
	${}^2L^{liquid}_{Co,Nb} = +26144.3$	[19]
	${}^0L^{liquid}_{Co,Zr} = -153092.0 + 14.484T$	[27]
	${}^1L^{liquid}_{Co,Zr} = -12768.0$	[27]
	${}^2L^{liquid}_{Co,Zr} = +34316.0 - 5.594T$	[27]
	${}^0L^{liquid}_{Nb,Zr} = +10311.0$	[29]
	${}^1L^{liquid}_{Nb,Zr} = +6709.0$	[29]
	${}^0L^{liquid}_{Co,Nb,Zr} = -16150.0$	this work
	${}^1L^{liquid}_{Co,Nb,Zr} = -16500.0$	this work
	${}^2L^{liquid}_{Co,Nb,Zr} = -8965.0$	this work
bcc	$(Co,Nb,Zr,Va)_1(Va)_3$	
	${}^0L^{bcc}_{Co,Va} = +165000.0$	[19]
	${}^0L^{bcc}_{Co,Nb} = -10599.7 - 3.274T$	[19]
	${}^0L^{bcc}_{Co,Zr} = -55065.0$	[27]
	${}^1L^{bcc}_{Co,Zr} = +3500.0$	[27]
	${}^0L^{bcc}_{Nb,Va} = +135000 - 0.200RT$	[19]
	${}^0L^{bcc}_{Zr,Va} = +320000.0$	[27]
	${}^0L^{bcc}_{Va,Va} = +30.000T$	[27]
	${}^0L^{bcc}_{Nb,Zr} = +15911.0 + 3.350T$	[29]
	${}^1L^{bcc}_{Nb,Zr} = +3919.0 - 1.09T$	[29]
	${}^0L^{bcc}_{Co,Nb,Zr} = -12000.0$	this work
	${}^1L^{bcc}_{Co,Nb,Zr} = -12000.0$	this work
	${}^2L^{bcc}_{Co,Nb,Zr} = +12000.0$	this work
Co_7Nb_2	Co_7Nb_2	
	$G^{Co_7Nb_2}_{Co:Nb} = +7GHSER_{Co} + 27GHSER_{Nb} - 160728.2 + 4.843T$	[19]
$Co_{11}Zr_2$	$(Co)_{11}(Nb,Zr)_2$	
	$G^{Co_{11}Zr_2}_{Co:Zr} = +11GHSER_{Co} + 2GHSER_{Zr} - 299728.0 + 21.294T$	[27]
$Co_{23}Zr_6$	$(Co)_{23}(Nb,Zr)_6$	
	$G^{Co_{23}Zr_6}_{Co:Zr} = +23GHSER_{Co} + 6GHSER_{Zr} - 823571 + 26.506T$	[27]
	$G^{Co_{23}Zr_6}_{Co:Nb} = +23GHSER_{Co} + 6GHSER_{Nb} - 235000$	this work
	${}^0L^{Co_{23}Zr_6}_{Co:Nb,Zr} = +130155.0 - 210.000T$	this work
	${}^1L^{Co_{23}Zr_6}_{Co:Nb,Zr} = -71939.0 + 100.000T$	this work
	${}^2L^{Co_{23}Zr_6}_{Co:Nb,Zr} = +50764.0 - 150.000T$	this work
CoZr	$(Co,Nb,Zr,Va)_{0.5}(Co,Nb,Zr,Va)_{0.5}(Va)_3$	
	$L^{CoZr}_{Va:Va} = +30T$	[27]
	$L^{CoZr}_{Zr:Co} = L^{CoZr}_{Co:Zr} = +6112.0 + 7.137T$	[27]
	$G^{CoZr}_{Co:Va} = G^{CoZr}_{Va:Co} = +.5GHSER_{Co} + 53550.0$	[27]
	${}^0L^{CoZr}_{Co:Zr} = +62112.0 + 7.137T$	[27]
	$G^{CoZr}_{Zr:Va} = G^{CoZr}_{Va:Zr} = +.5GHSER_{Zr} + 44200.0$	[27]
	${}^0L^{CoZr}_{Co:Co,Zr} = {}^0L^{CoZr}_{Co,Zr:Co} = +49181.0$	[27]
	${}^0L^{CoZr}_{Zr:Co,Zr} = {}^0L^{CoZr}_{Co,Zr:Zr} = +91491.0$	[27]
	${}^0Tc^{CoZr}_{Co:Zr} = {}^0Tc^{CoZr}_{Zr:Co} = -1175.0$	[27]
	${}^0L^{CoZr}_{Co:Nb,Zr} = {}^0L^{CoZr}_{Nb,Zr:Co} = -52491.0$	this work
	${}^0L^{CoZr}_{Co,Nb:Zr} = {}^0L^{CoZr}_{Zr:Co,Nb} = +45626.0$	this work
	${}^0L^{CoZr}_{Co,Zr:Nb} = {}^0L^{CoZr}_{Nb:Co,Zr} = +48626.0$	this work
$CoZr_2$	$(Co,Zr)(Co,Nb,Zr)_2$	
	$G^{CoZr_2}_{Co:Zr} = +GHSER_{Co} + 2GHSER_{Zr} - 91215.0 + 0.969T$	[27]
	$G^{CoZr_2}_{Zr:Zr} = +3GHSER_{Zr} + 87000.0$	[27]
	${}^0L^{CoZr_2}_{Co,Zr:Zr} = -35000.0$	[27]
	$G^{CoZr_2}_{Co:Nb} = +GHSER_{Co} + 2GHSER_{Nb} + 36000.0$	this work

Table VI. continued

Phase	Thermodynamic Model and Parameter	References
	$G^{CoZr_2}_{Zr:Nb} = +GHSER_{Zr} + 2GHSER_{Nb} + 45000.0$	this work
	${}^0L^{CoZr_2}_{Co,Nb:Zr} = -9310.0 - 26.000T$	this work
	${}^1L^{CoZr_2}_{Co,Nb:Zr} = +9110.0 + 28.000T$	this work
	${}^2L^{CoZr_2}_{Co,Nb:Zr} = -9110.0 - 30.000T$	this work
$CoZr_3$	$(Co,Zr)(Co,Zr)Zr_2$	
	$G^{CoZr_3}_{Co:Co:Zr} = +2GHSER_{Co} + 2GHSER_{Zr} - 160540.0 + 6.012T$	[27]
	$G^{CoZr_3}_{Zr:Co:Zr} = +3GHSER_{Zr} + GHSER_{Co} - 98944.0 + 7.280T$	[27]
	$G^{CoZr_3}_{Co:Zr:Zr} = +GHSER_{Co} + 3GHSER_{Zr} - 98944.0 + 7.280T$	[27]
	$G^{CoZr_3}_{Zr:Zr:Zr} = +4GHSER_{Zr} + 16000.0 + 14.000T$	[27]
	${}^0L^{CoZr_3}_{Co:Co,Zr:Zr} = {}^0L^{CoZr_3}_{Co,Zr:Co:Zr} = +8166.0$	[27]
	${}^0L^{CoZr_3}_{Zr:Co,Zr:Zr} = {}^0L^{CoZr_3}_{Co,Zr:Zr:Zr} = -2214.0$	[27]
fcc	$(Co,Nb,Zr)_1(Va)_1$	
	${}^0L^{fcc}_{Co,Zr} = -60000.0$	[27]
	${}^1L^{fcc}_{Co,Zr} = -4000.0$	[27]
	${}^0L^{fcc}_{Co,Nb} = -35746.6 - 14.848T$	[19]
hcp	$(Co,Nb,Zr)_1(Va)_{0.5}$	
	${}^0L^{hcp}_{Co,Zr} = -47428.0$	[27]
	${}^1L^{hcp}_{Co,Zr} = -5961.0$	[27]
	${}^0L^{hcp}_{Nb,Zr} = +24411.0$	[29]
λ_1	$(Co,Nb)_2(Co,Nb)_1$	
	$G^{\lambda_1}_{Co:Co} = +3GHSER_{Co} + 53403.9$	[19]
	$G^{\lambda_1}_{Co:Nb} = +2GHSER_{Co} + GHSER_{Nb} - 61714.0 - 6.378T$	[19]
	$G^{\lambda_1}_{Nb:Co} = +GHSER_{Co} + 2GHSER_{Nb} + 62124.0 + 6.106T$	[19]
	$G^{\lambda_1}_{Nb:Nb} = +3GHSER_{Nb} + 15000.0$	[19]
	${}^0L^{\lambda_1}_{Co,Nb:Nb} = -6564.9$	[19]
	${}^1L^{\lambda_1}_{Co,Nb:Nb} = -12342.2$	[19]
λ_2	$(Co,Nb,Zr)_2(Co,Nb,Zr)_1$	
	$G^{\lambda_2}_{Co:Co} = +3GHSER_{CO} + 63136.8$	[19]
	$G^{\lambda_2}_{Co:Zr} = +2GHSER_{Co} + GHSER_{Zr} - 118425.0 + 2.355T$	this work
	$G^{\lambda_2}_{Zr:Co} = +GHSER_{Co} + 2GHSER_{Zr} + 148425.0 - 2.355T$	this work
	$G^{\lambda_2}_{Zr:Zr} = +3GHSER_{Zr} + 15000.0$	this work
	${}^0L^{\lambda_2}_{Co:Co,Zr} = -94668.0 + 12.750T$	this work
	${}^1L^{\lambda_2}_{Co:Co,Zr} = +28668.0$	this work
	$G^{\lambda_2}_{Nb:Co} = +GHSER_{Co} + 2GHSER_{Nb} + 93355.7 + 5.609T$	[19]
	$G^{\lambda_2}_{Co:Nb} = +2GHSER_{Co} + GHSER_{Nb} - 63355.7 - 5.684T$	[19]
	$G^{\lambda_2}_{Nb:Nb} = +3GHSER_{Nb} + 15000.0$	[19]
	${}^0L^{\lambda_2}_{Co:Co,Nb} = -96868.3 + 3.606T$	[19]
	${}^1L^{\lambda_2}_{Co:Co,Nb} = -41400$	[19]
	${}^0L^{\lambda_2}_{Co,Nb:Nb} = -1413.7$	[19]
	$G^{\lambda_2}_{Zr:Nb} = +GHSER_{Nb} + 2GHSER_{Zr} + 20000.0$	this work
	$G^{\lambda_2}_{Nb:Zr} = +2GHSER_{Nb} + GHSER_{Zr} + 20000.0$	this work
	${}^0L^{\lambda_2}_{Co:Nb,Zr} = -21776.0 + 10.000T$	this work
	${}^1L^{\lambda_2}_{Co:Nb,Zr} = -12209.0 + 10.000T$	this work
	${}^2L^{\lambda_2}_{Co:Nb,Zr} = +3305.0 - 5.000T$	this work
	${}^0L^{\lambda_2}_{Co:Co,Nb,Zr} = -120497.0 + 80.000T$	this work
	${}^1L^{\lambda_2}_{Co:Co,Nb,Zr} = -104340.0 + 80.000T$	this work
	${}^2L^{\lambda_2}_{Co:Co,Nb,Zr} = +3305.0 + 80.000T$	this work
λ_3	$(Co,Nb)_2(Co,Nb)_1$	
	$G^{\lambda_3}_{Co:Co} = +3GHSER_{Co} + 57341.1$	[19]
	$G^{\lambda_3}_{Co:Nb} = +2GHSER_{Co} + GHSER_{Nb} - 62497.5 - 4.485T$	[19]
	$G^{\lambda_3}_{Nb:Co} = +GHSER_{Co} + 2GHSER_{Nb} + 92747.5 + 4.323T$	[19]

Table VI. continued

Phase	Thermodynamic Model and Parameter	References
	$G^{\lambda_3}_{Nb:Nb} = +3GHSER_{Nb}+15000.0$	[19]
	${}^0L^{\lambda_3}_{Co:Co,Nb} = -83077.6$	[19]
	${}^1L^{\lambda_3}_{Co:Co,Nb} = -18730.9$	[19]
μ	$(Co,Nb,Zr)_1(Nb,Zr)_4(Co,Nb,Zr)_2(Co,Nb,Zr)_6$	
	$G^{\mu}_{Co:Nb:Co:Co} = +GFCC_{Co} + 4GHSER_{Nb} + 2GBCC_{Co} +6GFCC_{Co}-218031.2$	[19]
	$G^{\mu}_{Nb:Nb:Co:Co} = +GFCC_{Nb} + 4GHSER_{Nb} + 2GBCC_{Co} +6GFCC_{Co}-179971.1$	[19]
	$G^{\mu}_{Co:Nb:Nb:Co} = +GFCC_{Co} + 4GHSER_{Nb} + 2GHSER_{Nb} +6GFCC_{Co} - 282434.7 - 17.886T$	[19]
	$G^{\mu}_{Nb:Nb:Nb:Co} = +GFCC_{Nb} + 4GHSER_{Nb} + 2GHSER_{Nb} + 6GFCC_{Co} - 309283.9 - 7.591T$	[19]
	$G^{\mu}_{Nb:Nb:Nb:Nb} = +GFCC_{Nb} + 4GHSER_{Nb} + 2GHSER_{Nb} +6GFCC_{Nb}+126006.8$	[19]
	${}^0L^{\mu}_{Co:Nb:Co,Nb:Co} = -21922.8$	[19]
	$G^{\mu}_{Co:Nb:Nb:Zr} = +GHSER_{Co} + 6GHSER_{Nb} + 6GHSER_{Zr}$	this work
	$G^{\mu}_{Co:Zr:Nb:Zr} = +GHSER_{Co} + 2GHSER_{Nb} + 10GHSER_{Zr}$	this work
	$G^{\mu}_{Co:Zr:Nb:Co} = +7GHSER_{Co} + 2GHSER_{Nb} + 4GHSER_{Zr} -326190.0 + 10.000T$	this work
	$G^{\mu}_{Nb:Zr:Nb:Co} = +6GHSER_{Co} + 3GHSER_{Nb} + 4GHSER_{Zr} -214990.0 + 10.000T$	this work
	$G^{\mu}_{Nb:Zr:Nb:Nb} = +9GHSER_{Nb} + 4GHSER_{Zr} + 38000.0$	this work
	$G^{\mu}_{Nb:Zr:Nb:Zr} = +3GHSER_{Nb} + 10GHSER_{Zr} + 38000.0$	this work
	$G^{\mu}_{Nb:Nb:Nb:Zr} = +7GHSER_{Nb} + 6GHSER_{Zr} + 38000.0$	this work
	${}^0L^{\mu}_{Co:Nb,Zr:Nb:Co} = -138540.0 - 50.000T$	this work
	${}^1L^{\mu}_{Co:Nb,Zr:Nb:Co} = +29730.0 + 50.000T$	this work
	${}^2L^{\mu}_{Co:Nb,Zr:Nb:Co} = +175680.0 - 100.000T$	this work
	${}^0L^{\mu}_{Nb:Nb,Zr:Nb:Co} = -217190.0 + 20.000T$	this work
	${}^1L^{\mu}_{Nb:Nb,Zr:Nb:Co} = -206435.0 + 50.000T$	this work
	${}^2L^{\mu}_{Nb:Nb,Zr:Nb:Co} = -68165.0 + 150.000T$	this work
	${}^0L^{\mu}_{Co,Nb:Zr:Nb:Co} = -219730.0 - 120.000T$	this work
	${}^1L^{\mu}_{Co,Nb:Zr:Nb:Co} = -111080.0 - 80.000T$	this work
	${}^2L^{\mu}_{Co,Nb:Zr:Nb:Co} = -111080.0 - 80.000T$	this work

In J mol^{-1} of the formula units.

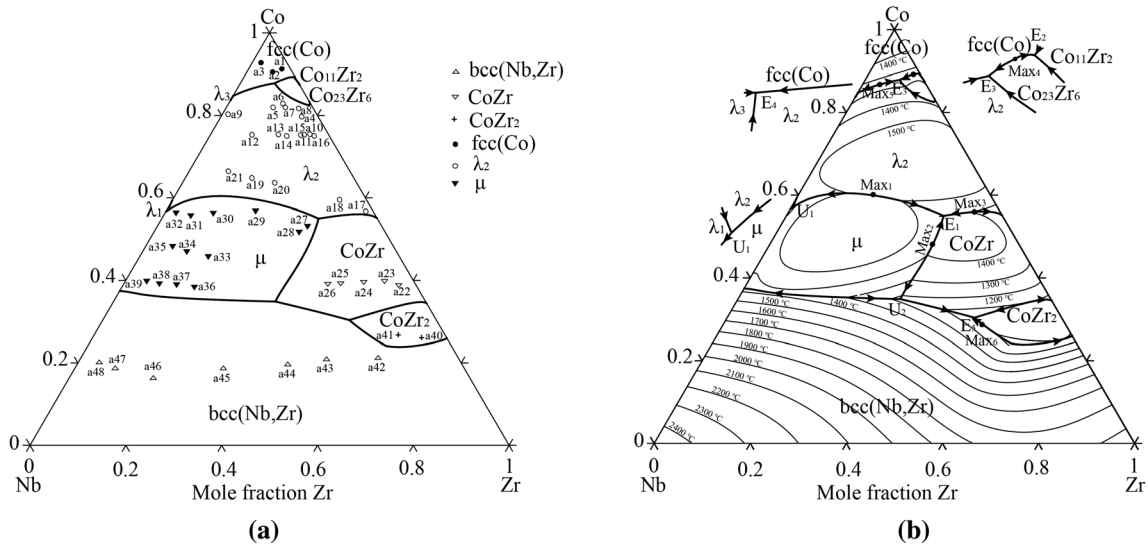

Fig. 16—Calculated liquidus surface projection of the Co–Nb–Zr system with: (*a*) experimental data; (*b*) isothermal lines.

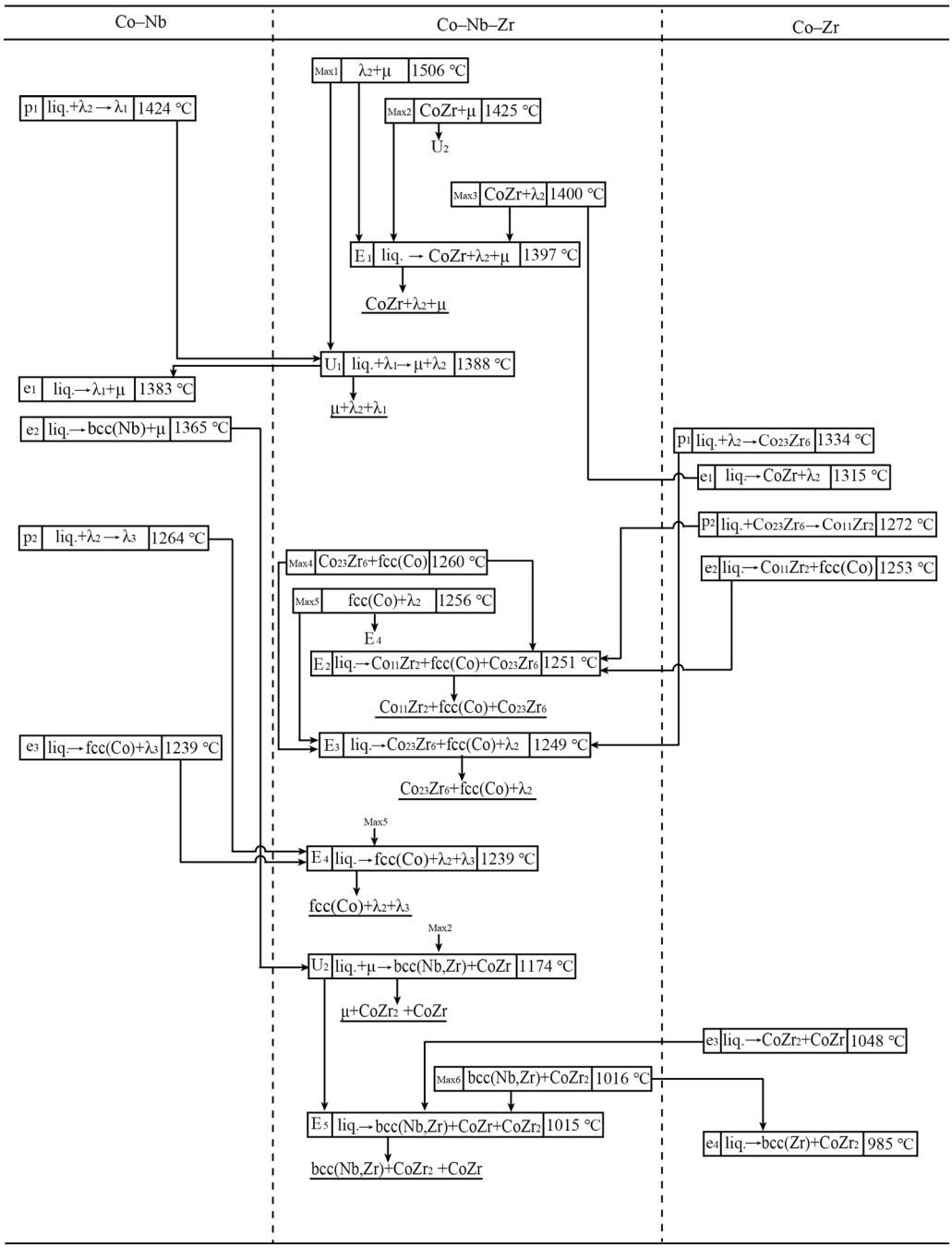

Fig. 17—Invariant reaction scheme in the Co–Nb–Zr system.

Table VII. Calculated Invariant Reactions of the Co–Nb–Zr System

Reactions	Type	T (°C)	Compositions of Liquid (At. Pct)		
			Co	Ta	Zr
Liq. → CoZr + λ_2 + μ	E_1	1399	55.0	12.3	32.7
Liq. + λ_2 → λ_1 + μ	U_1	1384	57.1	42.7	0.2
Liq. → $Co_{11}Zr_2$ + $Co_{23}Zr_6$ + fcc(Co)	E_2	1251	89.3	0.3	10.4
Liq. → $Co_{23}Zr_6$ + fcc(Co) + λ_2	E_3	1249	87.8	5.0	7.2
Liq. → fcc(Co) + λ_2 + λ_3	E_4	1239	84.7	15.3	0.0
Liq. + μ → bcc(Nb,Zr) + CoZr	U_2	1174	34.9	31.3	33.8
Liq. → bcc(Nb,Zr) + $CoZr_2$ + CoZr	E_5	1012	30.4	18.2	51.4

ACKNOWLEDGMENTS

this work was supported by Beijing Natural Science Foundation (Grant No. 2232077), National Natural Science Foundation of China (NSFC) (Grant No. 52271002) and the Cooperation Project of Jiangxi Provincial International Science and Technology (Grant No. 20212BDH81001).

CONFLICT OF INTEREST

On behalf of all authors, the corresponding author states that there is no conflict of interest.

REFERENCES

1. J. Zhao, F. Ma, P. Liu, X. Liu, W. Li, and D. He: *J. Mater. Eng. Perform*., 2020, vol. 29, pp. 3736–44.
2. T. Nagase, Y. Iijima, A. Matsugaki, K. Ameyama, and T. Nakano: *Mater. Sci. Eng. C*, 2020, vol. 107, p. 110322.
3. Z. Han, X. Liu, S. Zhao, Y. Shao, J. Li, and K. Yao: *Prog. Nat. Sci. Mater*., 2015, vol. 25, pp. 365–69.
4. T. Omori, K. Oikawa, J. Sato, I. Ohnuma, U.R. Kattner, R. Kainuma, and K. Ishida: *Intermetallics*, 2013, vol. 32, pp. 274–83.
5. I. Povstugar, P.P. Choi, S. Neumeier, A. Bauer, C.H. Zenk, M. Göken, and D. Raabe: *Acta Mater*., 2014, vol. 78, pp. 78–85.
6. X. Liu, Y. Pan, Y. Chen, J. Han, S. Yang, J. Ruan, C. Wang, Y. Yang, and Y. Li: *Metals*, 2018, vol. 8, p. 563.
7. S.G. Huang, R.L. Liu, L. Li, O.V. Der Biset, and J. Vleugels: *Int. J. Refract. Met. H Mater*., 2008, vol. 26, pp. 389–95.
8. D.A. Sandoval, J.J. Roa, O. Ther, E. Tarrés, and L. Llanes: *J. Alloys Compd*., 2019, vol. 777, pp. 593–601.
9. X. Liu, C. Luo, M. Yang, S. Yang, J. Zhang, Y. Huang, J. Han, Y. Lu, and C. Wang: *J. Phase Equilib. Diffus*., 2020, vol. 41, pp. 3–14.
10. W. Gui, H. Zhang, M. Yang, T. Jin, X. Sun, and Q. Zheng: *J. Alloys Compd*., 2017, vol. 695, pp. 1271–78.
11. Y. Liu, L. Zhang, T. Pan, D. Yu, and Y. Ge: *CALPHAD*, 2008, vol. 32, pp. 455–61.
12. J. Ågren: *Curr. Opin. Solid State Mater. Sci*., 1996, vol. 1, pp. 355–60.
13. H. Okamoto: *J. Phase. Equilib*., 2000, vol. 21, p. 495.
14. F. Stein, D. Jiang, M. Palm, G. Sauthoff, D. Grüner, and G. Kreiner: *Intermetallics*, 2008, vol. 16, pp. 785–92.
15. K.C.H. Kumar, I. Ansara, P. Wollants, and L. Delaey: *J. Alloys Compd.*, 1998, vol. 267, pp. 105–12.
16. C. He, F. Stein, and M. Palm: *MRS Online Proceedings Library (OPL)*, 2008, p. 1128.
17. L. Zhou, C. Wang, Y. Yu, X. Liu, H. Chinen, T. Omori, R. Kainuma, and K. Ishida: *J. Alloys Compd*., 2011, vol. 509, pp. 1554–62.
18. C. He, F. Stein, and M. Palm: *J. Alloys Compd*., 2015, vol. 637, pp. 361–75.
19. D. Wei, X. Bai, C. Guo, R. Li, and Z. Du: *J. Alloys Compd*., 2022, vol. 924, 166516.
20. W.H. Pechin, D.E. Williams, and W.L. Larsen: *Am. Soc. Met. Trans. Q*., 1964, vol. 57, p. 744.
21. S.K. Bataleva, V.V. Kuprina, V.V. Burnasheva, V.Y. Markiv, and G.N. Ronami: *Moscow Univ. Chem. Bull*., 1970, vol. 25, pp. 33–36.
22. X. Liu, H. Zhang, C. Wang, and K. Ishida: *J. Alloys Compd*., 2009, vol. 482, pp. 99–105.
23. A. Durga and K.C. Kumar: *CALPHAD*, 2010, vol. 34, pp. 200–05.
24. A. Durga, K.C. Kumar, N. Moelans, and P. Wollants: *J. Alloys Compd*., 2010, vol. 334, pp. 173–81.
25. T. Kosorukova, P. Agraval, V. Ivanchenko, and M. Turchanin: in *XI International Conference on Crystal Chemistry of Intermetallic Compounds*, 2010, p. 52.
26. J.C. Gachon and J. Hertz: *CALPHAD*, 1983, vol. 7, pp. 1–2.
27. C. Zhou and H. Wang: *J. Phase Equilib. Diffus*., 2021, vol. 42, pp. 77–90.
28. A.F. Guillermet: *Int. J. Mater. Res*., 1991, vol. 82, pp. 478–87.
29. J. Li, Y. Guo, S. Yang, Z. Shi, C. Wang, and X. Liu: *J. Alloys Compd*., 2015, vol. 642, pp. 216–24.
30. A.A. Kodentsov, G.F. Bastin, and F.J.J. van Loo: *J. Alloys Compd*., 2001, vol. 320, pp. 207–17.
31. A.T. Dinsdale: SGTE Pure ELEMENTS (Unary) Database, version 4.5, 2006.
32. O. Redlich and A.T. Kister: *Ind. Eng. Chem*., 1948, vol. 40, pp. 345–48.
33. J. Sun, C. Ming, B. Yang, C. Guo, C. Li, and Z. Du: *J. Alloys Compd*., 2023, vol. 939, 168696.